ANNUAL REPORT

for NASA grant NAGW 3543 titled

SeaWiFS CALIBRATION AND ALGORITHM VALIDATION

Submitted by:

Robert J. Parada, Jr.
Graduate Student

Philip N. Slater
Principal Investigator

Remote Sensing Group
Optical Sciences Center
University of Arizona
Tucson, Arizona 85721

October 1995

Table of Contents

INTRODUCTION AND SUMMARY

This is the third annual report on NASA grant NAGW 3543, titled "SeaWiFS Calibration and Algorithm Validation" covering the period October 1, 1994 to October 31, 1995.

A substantial amount of field research has been completed during this period. The applicability of different in-flight calibration methods was studied. In addition, various field instruments and new equipment were tested to appraise their usefulness during such calibration activities. The majority of this work was conducted in the month of June. The persons primarily responsible for organizing this field work were K. Thome, an assistant professor in Optical Sciences, and R. J. Parada, Jr., a graduate student in the Remote Sensing Group (RSG). The purposes and (expected) results of these field experiments are detailed in separate sections of this report. One section contains a synopsis of calibrations conducted over both land and water targets. A second section contains the results of an experiment conducted to determine the spatial uniformity of surface reflectance at Lake Tahoe, the chosen water calibration site. Other research agencies/groups which collaborated with the RSG in these endeavors include a group from the Jet Propulsion Laboratory (JPL) headed by R. Green, a group from the the Naval Research Laboratory (NRL) headed by C. Davis, a team from K. Carder's research group at the University of South Florida (USF) headed by B. Steward, and the Tahoe research group of U. C. Davis headed by B. Richards.

Advances were also made in the area of radiative transfer software development. The work was accomplished primarily by R. Santer, a professor at the Laboratoire d'Optique Atmosphérique (LOA) in Lille, France. During a five-week period in July-August, Santer modified an existing *exact* radiative transfer code, Successive Orders (SO), to provide outputs of the radiance distribution at arbitrary altitudes above a selected calibration target. These modifications were needed to utilize the SO software in radiance-based sensor calibrations.

In addition to these accomplishments, serious thought was also given to the general applicability of various calibration techniques to calibrations conducted over water surfaces. In particular, the practicality of the *radiance-based* and *reflectance-based* methods of in-flight radiometric calibration was evaluated. The results of this evaluation, as well as certain algorithms used to determine the relative effects of the probabilistic sunglint radiance term, are included with this report in the form of a preprinted paper, "On the in-flight vicarious calibration of radiometric sensors over water targets," which was written by R. J. Parada, Jr.

R. J. Parada, Jr. also had the opportunity to attend a summer course in bio-optical oceanography offered at Friday Harbor Laboratories, a remote-facility associated with the University of Washington. This course provided an overall view of the principles, equipment, and current research focuses in the field of quantitative oceanography. Notable scientists such as M. J. Perry, N. McCormick, C. Roesler, C. Mobley, and K. Carder were featured lecturers. Included in the course instruction were discussions of the ways in which data retrieved from

ocean-viewing satellite sensors, such as SeaWiFS, will be of benefit to the scientific community.

In the months to come, a number of objectives have been earmarked for completion. Foremost among these is the continued reduction and analysis of the data collect from the past summer's field experiments. These results will serve as an indicator of which methodologies tend to provide the most consistent and reliable calibrations, and the targets over which the techniques are most applicable. In addition, based on the inevitable equipment difficulties encountered during the field experiments, a number of improvements to the existing radiometers, the associated electronics and power supplies, and the mounting hardware are being carried out. R. J. Parada, Jr. will be spending a period of approximately six months in France beginning in January of 1996. While there, he will work with R. Santer on performing an in-depth sensitivity analysis of the radiative transfer code SO, which is to be used during all future in-flight calibrations of the SeaWiFS sensor. The RSG will be hiring a post-doctorate person to carry on work in Tucson associated with the calibration of SeaWiFS. The launch of SeaWiFS is, at this point, anticipated for June of 1996. The first in-flight calibration campaign is therefore tentatively being planned for late June or early July at Lake Tahoe.

June 1995 In-Flight Vicarious Sensor Calibration Experiments

Robert J. Parada, Jr.
Remote Sensing Group, Optical Sciences Center, University of Arizona
Tucson, Arizona 85721

1.0 Introduction

The calibration experiments discussed herein were conducted during the period from June 20, 1995 to June 22, 1995. The locations used were Ivanpah Playa, Nevada and Lake Tahoe, California-Nevada. Much of the data from this fieldwork is still in the process of being reduced. Therefore, only a preliminary discussion is presented - with a more in-depth description being deferred to a future report.

2.0 Sensor Description and Instrumentation Synopsis

The June calibration experiments involved the Airborne Visible/Infrared Imaging Spectrometer (AVIRIS) and the Hyperspectral Digital Imagery Collection Experiment (HYDICE) systems. AVIRIS is a whisk-broom system using linear arrays. It covers the spectral range from 0.4 μm to 2.5 μm. There are four separate spectrometers in the system (one composed of silicon and three composed of Indium Antimonide) which afford continuous sampling of the stated spectral range in 226 separate channels at band spacings of 100 nm. The device has an angular instantaneous field-of-vierw (IFOV) of 1 mrad, which translates to a 20 m ground linear IFOV, and a 10.5 km swath width for an altitude of 20 km at which it is typically flown. [It is worth noting, however, that the sensor may also be flown low enough to produce a 3 m footprint.] HYDICE is a pushbroom system using a monolithic two-dimensional focal array composed of Indium Antimonide. It covers the spectral range from 0.4 μm to 2.5 μm. The 206 channels have bandwidths ranging from 3.1 nm to 14.9 nm. The device has a 0.5 mrad angular IFOV. Note that the broad spectral response of each sensor encompasses the spectral range covered by the SeaWiFS sensor.

AVIRIS is a more-established sensor controlled by the Jet Propulsion Laboratory (JPL) which had been calibrated in the field on numerous occasions prior to the June calibration experiments. HYDICE, on the other hand, is a relatively new sensor under the development of the Naval Research Laboratory (NRL) in conjunction with Hughes Danbury Optical Systems, Inc. which had yet to be calibrated in the field at the time of the June calibration experiments.

The calibration instrumentation used by the Remote Sensing Group (RSG) can be broken down into two categories: (1) instrumentation used during *reflectance-based* calibrations; (2) instrumentation used during *radiance-based* calibrations.

For reflectance-based calibrations, the RSG employs a Reagan solar radiometer to collect total atmospheric optical depth measurements. In conjunction with this radiometer, a variety of meteorological instruments are used which provide information on Rayleigh optical depths, total downwelled irradiance, and relative humidity and temperature for future corrections of the optical depth measurements. Also used is a water vapor meter which provides information about the total columnar water vapor absorption. In addition to these optical depth related instruments, the RSG employs radiometers for measuring the spectral reflectance of a selected calibration target. During the June campaign, an ASD spectrometer and an Exotech radiometer were used to collect this information. Finally, the RSG employs canvas reflectance standards having known, spectrally-flat reflectances for use both as localized targets and for image registration purposes.

For radiance-based calibrations, the RSG employs several radiometers to collect upwelled spectral radiances at a certain altitude above a selected calibration target. The radiometers used during the June campaign were a Barnes MMR radiometer, a Spectron spectroradiometer, and a customized absolutely calibrated radiometer designed by S. Biggar of the RSG. In addition to these radiometers, a small video camera was used to acquire imagery of the area overflown by the sensors. This aided in image/signal registration. These instruments were loaded aboard a Cessna-180 aircraft flown by C. Curtis, a research professor in the Physics department at the University of Arizona. They were mounted in a customized rigging built specifically for the purpose of calibrating SeaWiFS using the radiance-based method. The initial design for this mount was created by R. J. Parada, Jr. and the construction was carried out by the Optical Machine Shop of the Optical Sciences Center at the University of Arizona.

3.0 Calibrations Conducted Over A (High-Reflectance) Land Target

Reflectance-based and radiance-based calibrations of the stated sensors were conducted over Ivanpah Playa. This location is a rather bright reflectance, sandy region located close to the California-Nevada border. Groups from JPL and NRL were involved with the RSG in these activities. The site was chosen by the JPL calibration team after Lunar Lake, Nevada (the intended target) was found to contain standing water from unusually heavy spirng rains. This decision was made both because of the proximity of the playa to the JPL home base and because the site had been used by that group during previous in-flight calibrations of AVIRIS.

During the overflights of the two sensors, the Cessna-180 airplane used by the RSG made several passes over the calibration site. The instruments on board this aircraft collected spectral radiance information at an altitude of approximately 3,650 m above mean sea level. This was about 2,860 m above the target. Radiance data were collected along the AVIRIS flight line, which differed slightly from the HYDICE flight line. A reflectance-based calibration of HYDICE was able to be directly accomplished. It is possible that a radiance-based calibration of HYDICE may also be accomplished after careful registration the

collected aircraft data using the simultaneously collected video imagery. However, the target area used by HYDICE seldom fell within the flown radiometers' fields-of-view. An alternative is to first conduct a radiance-based calibration of AVIRIS and to then use the calibrated AVIRIS data to cross-calibrate HYDICE. This is possible since the AVIRIS imagery contains the calibration target area overflown by HYDICE as well as the target area overflown by the RSG calibration radiometers.

At the present time, a reflectance-based calibration of HYDICE has been completed by the RSG and a reflectance-based calibration of AVIRIS has been completed by JPL. In addition, the radiometer data collected over during the calibration overflights has been organized. However, the imagery collected by AVIRIS and HYDICE has not yet been viewed and co-registered with this data. After this has been done, radiance-based calibrations may be completed, and the results compared with those from the reflectance-based calibrations. If shown effective, radiance-based calibrations conducted over high-reflectance targets will be proven a reliable method by which to calibrate SeaWiFS using the upper arm of the sensor's bi-linear gain. Use of the radiance-based method of calibration has the advantage of having smaller predicted radiometric uncertainties than the reflectance-based method (i.e. 2.8% as opposed to 4.9%), and so is the preferred calibration technique. These uncertainties are expected to be reduced (i.e. to 1.8% and 3.3%) in the next two years as further improvements are made to the methods.

During this measurement period, a number of practical considerations were noted which need to be addressed prior to the calibration of SeaWiFS using a radiance-based calibration technique. First, the need to better isolate the flown radiometers from aircraft vibrations became apparent. Second, the use of multiple computers to handle the various flown radiometers became logistically very difficult to manage. A simpler means of handling datalogging from multiple instruments needs to be implemented. Third, there is a need to reduce the amount of power consumed by the instruments and their associated electronics in order to extend the length of the useful data collection period. Finally, there is a need to determine ways by which to more accurately synchronize the various sensor signals. During the June experiments, each sensor had its own separate time index. These were co-registered by use of the simultaneously collected video imagery and the airplane GPS data.

4.0 Calibrations Conducted Over A (Low-Reflectance) Water Target

The AVIRIS and HYDICE sensors also collected imagery over Lake Tahoe this past June. Multispectral radiances were collected by the RSG at an altitude of approximately 3,650 m above mean sea level. This is about 1,750 m above the lake surface. Atmospheric information and lake windspeed measurements were also recorded. A contingent from the University of South Florida (USF) was on-hand to collect in-water measurements along with remotely-sensed reflectances from the lake surface.

The data collected by the RSG have been organized. At the present time, the group is still waiting to receive the imagery collected by AVIRIS and HYDICE. After receiving the data, the corresponding radiance-based calibrations of the sensors over this dark (i.e. low-reflectance) target will be completed, and the results compared with those from the reflectance- and radiance-based calibrations conducted at Ivanpah Playa. If shown effective, radiance-based calibrations conducted over low-reflectance targets will be proven to be a reliable method by which to calibrate SeaWiFS in the lower arm of the sensor's bi-linear gain. This is an important distinction from calibrations conducted over high-reflectance targets for two reasons. First, the lower arm of the bi-linear gain is the portion of the sensor's dynamic range in which most of the quantitative measurements of water color and retrieval of in-water constituents will be made. It is therefore more appropriate to calibrate the sensor using this portion of the gain. Second, calibrating the instrument in both the lower- and upper-arm of the gain will yield a means of confirming the relationship between these two gain regions.

During the course of this measurement period, it was observed that a strange scatter component was present on the surface of the lake. Since Lake Tahoe had been chosen as a possible target for upcoming in-flight calibrations of SeaWiFS, an effort was made to better understand the nature of this unexpected surface scatter. A description of the experiment conducted and the preliminary results obtained from the associated study are contained in a separate section of this report.

Spatial Uniformity of Surface Reflectance for Lake Tahoe: A Preliminary Report

Robert J. Parada, Jr.
Remote Sensing Group, Optical Sciences Center, University of Arizona
Tucson, Arizona, 85721

Abstract

A preliminary study of an unexpected scatter component present on the surface of Lake Tahoe during the month of June, 1995 is presented. The general spectral nature of this phenomenon has been investigated and it's effects on surface uniformity and on expected at-sensor radiances has been shown to be sizeable. Possible explanations for this strange surface feature are presented, though at the present time confirmation is lacking. The observed effect is important in relation to the SeaWiFS sensor since Lake Tahoe has been selected as a possible target for use during in-flight radiometric calibrations of the sensor.

1.0 Introduction

During recent calibration experiments conducted over Lake Tahoe, a strange reflectance/scatter effect was observed on the lake surface. The lake appeared as though its surface was covered with some sort of highly-diffuse scattering layer. This "layer" was seen to be very patchy over the spatial extent of the lake.

In an effort to better understand this phenomenon, a spatial uniformity experiment was conducted. The reason for carrying out this study stems from the decision to use Lake Tahoe as a calibration site for upcoming in-flight calibrations of the SeaWiFS sensor. More specifically, this investigation is very important since spatial nonuniformities result in an inhomogeneous boundary layer. This condition is difficult to compensate for in sensors, such as SeaWiFS, having a large footprint since small scale surface features are undersampled. A study of surface uniformity therefore helps evaluate the extent to which such features might be problematic in calibrations conducted over Lake Tahoe.

2.0 Methods

On June 23, 1995 an aircraft-based sampling of the upwelling radiance over Lake Tahoe was made. For this survey, a Barnes MMR radiometer was used to collect the upwelling spectral radiances at an altitude of approximately 3,650 m above mean sea level. This is about 1,750 m above the lake surface. This radiometer has eight bands covering the spectral range from 0.45 μm to 12.5 μm. Only the first seven bands, which encompass the spectral range from 0.45 μm to 2.35 μm, were used in this study. A summary of these bands

is given in Table 1. The full field-of-view for each channel is approximately one degree.

Data collection took place between 11:00 am and 12:00 pm Mountain Standard Time (MST). The aircraft used for the study was a Cessna-180 airplane flown by C. Curtis, a research professor in the Physics department at the University of Arizona. The instrumentation was operated by R. J. Parada, Jr. of the Remote Sensing Group (RSG). The data were collected in a pseudo-raster fashion over the surface of the lake with the radiometer pointed in the downward vertical direction. An exact flight-path, shown both in three-dimensions and projected onto the ground surface, is shown in Figure 1. This flight path has been reconstructed from the actual GPS signal recorded by the aircraft during the course of the experiment. In all, five passes were made over the lake, running along north-south tracks. Due to equipment failure, only the first four passes produced useful information. The final pass was over the shallow western part of the lake, in which the bottom reflectance is clearly visible. This portion of the lake is therefore unsuitable for calibration purposes and is not of great importance to the current study.

Several corrections were made to the resulting radiance data. First, the average dark levels were subtracted from each of the recorded signal voltages. Following this, a correction for the gain factors used for each channel was made. After this, the calibration coefficients for each channel were used to convert the corrected signal voltages to radiances. The resultant formula showing these various corrections is given in Equation 1.

$$L_n = \frac{1}{A_n}\left(\frac{V_n - V_{dark_n}}{G_n}\right) \tag{1}$$

In this expression, L_n represents the total upwelled radiance in band n, A_n represents the calibration coefficient in units of volts/radiance, V_n represents the recorded voltage in band n, $Vdark_n$ represents the associated dark voltage in band n, and G_n represents the gain setting used for band n.

In order to retrieve the lake reflectance values from the upwelled radiances, a number of atmospheric corrections were also made to the data. By utilizing an approximate radiative transfer code, based on the program *Simulation of the Satellite Signal in the Solar Spectrum* (5S) written by Tanre et al, the atmospheric path radiance was calculated for the solar-sensor geometry involved in the experiment. For these radiative transfer code runs, a typical lake surface was assumed. In addition, a continental aerosol model was employed. The radiances due to the atmosphere alone were calculated for each band. These values were then subtracted from the total upwelled radiance in the corresponding band.

Following this atmospheric correction, the effective Lambertian reflectance was calculated. This figure-of-merit (FOM) was selected to provide a means by which to judge

the uniformity of the lake reflectance. This FOM has an obvious drawback: the reflectance of a water surface is largely specular. The lake reflectance approaches being Lambertian only well outside the region of sunglint. For the solar-sensor geometry present during the course of the data collection, the sensor view angle was outside the region of sunglint. Therefore, the chosen FOM allows the determination of which regions on the lake behave normally and which have some anomalous scattering component. The combined formula used to compute this effective reflectance is shown in Equation 2.

$$\rho_{eff} = \pi \left(\frac{L_n - L_{atmos_n}}{E_n} \right) \tag{2}$$

In this expression for effective reflectance, ρ_{eff}, the factor of π implies the assumption that the measured reflectance is equal in all directions within the upward hemisphere, L_n represents the total radiance in band n, $Latmos_n$ represents the atmospheric contribution to upwelled radiance in band n, and E_n is the total downwelled irradiance at the lake surface. This final quantity was again calculated by multiple runs of the modified 5S radiative transfer code.

Strictly speaking, at least one more correction should be made to this FOM. There is a relatively significant contribution to the upwelled radiance from the surface which is due to specular reflection of the vertically downwelled radiance back in the direction of the radiometer. Small increases in this downward radiance occurred during the measurement period due to a change in the solar zenithal angle. This had the effect of slightly biasing the later measurements to a higher reflectance level. By subtracting the specularly reflected radiance component, assuming a nominal reflectance coefficient, this bias may be removed.

3.0 Results

The resulting average reflectances, standard deviations, and associated uncertainties (taken to be the ratio of the standard deviation to the average reflectance) for each band are given in Table 2. This table contains the results for the individual passes made over the lake surface, and for the lake overall.

The resultant band reflectances for pass #1 (a longitude of 119.98 degrees West) are shown in Figure 2. The resultant band reflectances for pass #2 (a longitude of 120.02 degrees West) are shown in Figure 3. The resultant band reflectances for pass #3 (a longitude of 120.05 degrees West) are shown in Figure 4. The resultant band reflectances for pass #4 (a longitude of 120.08 degrees West) are shown in Figure 5.

Band reflectance spectra computed for a lake latitude at which normal water reflectances were observed in shown in Figure 6a. The latitude at which the most uniform water was observed was around 39.20 degrees North. Band reflectance spectra computed for a lake latitude at which the heightened scatter was present is shown in Figure 6b. The latitude for which this high-scatter spectrum was computed was 39.00 degrees North.

An image of a northern section of the lake taken from band #31 of an AVIRIS quicklook image (downloaded from the World Wide Web AVIRIS homepage) is include as Figure 7. This image was collected during the AVIRIS overflight of Lake Tahoe on June 22, 1995.

4.0 Analysis

One of the most immediately obvious results of this study is the relatively large uncertainty in effective reflectance as calculated using Equation 2. These uncertainties are listed in Table 2 and range from 0.2384 in band 1 (pass #1) to 1.0000 in band 4 (pass #4). The corresponding variance in reflectance is therefore seen to be considerable. [It should be noted that areas of unquestionably deviant reflectances, for example those of the lake shore boundary and those in the middle of pass #4, were not included in the computations of lake reflectance statistics.]

The large variance in band reflectances are illustrated graphically in Figures 2 through 5. Note that the spatial variability in reflectance is consistent between the seven bands of the radiometer. This consistency confirms that the variations are due to actual changes in surface reflectance rather than from internal instrument noise - since the noise in a given band is independent from that in the other bands.

Also apparent in Figures 2 through 5 is the presence of an area of relatively uniform reflectance. This area is located at the northern end of the lake. In contrast to this localized region of uniform reflectance, the remainder of the lake appears to vary significantly in its reflectance characteristics and, in general, has a higher degree of scatter from the surface. By viewing a spectral analysis of these disparate regions, some interesting trends are seen. These trends are shown in Figures 6a and 6b. The spectra of the uniform region is highly weighted toward the first band of the MMR radiometer. This band, as summarized in Table 1, encompasses the short-wavelength end of the visible spectrum. In other words, the radiance reflected from the water surface in this region appears bluish in color. This matches visual observation of the region. The spectra taken from a region having a high degree of scatter is much more flat. This implies that the radiance reflected from the lake surface is rather white, which is in agreement with visual observations of these regions.

Another trend which is apparent ,both from the summarized reflectance statistics and the graphed reflectance spectra, is that the average reflectance in each band tends to increase with each pass over the lake. This may be due to the actual lake reflectance, but it seems

more likely that the trend is due to the change in solar zenithal angle as a function of time. For each successive pass, the solar zenith decreased as the time approached solar noon. The scatter on the lake surface had the effect of diffusely reflecting the direct solar radiation into a range of directions - in essence, decreasing the specular nature of the lake reflectance. As the sun approached solar noon, two effects combined to cause the observed increase in reflectance: (1) the atmospheric transmittance of direct solar irradiance increased due to a decrease in optical path length; (2) the amount of direct solar radiation diffusely reflected into the upward vertical direction (i.e. toward the radiometer) increased as the sun moved closer to its apex.

Finally, one can get a general feel for the striated nature of the heightened-scatter "layer" on the surface of the lake by viewing Figure 7. In this figure, which shows a region of water near the northern end of the lake, regions of both clear (i.e. uniform) reflectance and heightened-scatter reflectance can be clearly seen. Note the general string-like nature of the regions of heightened scatter.

Explanations for the presence of the heightened-scatter region on the lake surface have thus far been varied. The author wishes to thank the following people for their kind insights to the problem: B. Richards, M. J. Perry, C. Roesler, K. Carder, B. Steward, C. Davis, and R. Santer. These people have provided instructive hypotheses and/or volunteered in-water measurements made around the period in which the uniformity study was made. After polling the various opinions offered, the following hypothesis seems at the moment to be the most likely explanation. This year, the majority of annual runoff from snowmelt occurred rather late - happening somewhere between June 19 and June 29. This period has been set by Secchi depth measurements taken by the local UC Davis research group headed by B. Richards. [Note that this period encompasses June 23, the date the uniformity experiment was conducted.] Relatively shallow Secchi depths were recorded between during this period and the cause was believed to be inorganic sediment from the snowmelt runoff. Such sediment could conceivably be one source of the heightened-scatter layer on the lake surface. This explanation is not completely satisfactory since, as pointed out by R. Santer, such sediment is not highly reflective in the near infrared portion of the electromagnetic spectrum and therefore would not explain the relative flatness of the reflectance spectrum in the upper bands of the MMR radiometer. It is conceivable that the increased amount of inorganic sediments added to the lake from the runoff supplied needed nutrients to one or more species of phytoplankton which, in turn, bloomed near the surface of the lake and produced the observed scatter. Measurements made on June 29 by the research group of B. Richards seems to support the presence of *animal* plankter known as rotifers in the lake at that time.

It should be pointed out that the amalgamated hypothesis presented has yet to be confirmed with in-water measurements taken closer to the date the study was conducted. Such data have been graciously volunteered by groups from the Naval Research Laboratories (NRL), and the University of South Florida (USF). At the present time, this information has not been received, but is expected to be available in the near future.

5.0 Conclusions

The results of this experiment clearly indicate that the unexpected scatter from the surface of Lake Tahoe is a definite problem if that lake is to be used as a low-reflectance calibration target. Luckily, this heightened scatter seems to be localized to a short period of time during the year so that, should proper care be given to selecting the period in which calibrations are to be performed, this phenomenon may be avoided.

Further investigation needs to be made into the true cause of this increased lake scatter. It is recommended that closer affiliation be made with both the research team of UC Davis headed by B. Richards, the research team at USF headed by K. Carder, and the research contingent from the NRL headed by C. Davis.

TABLE 1: Summary of Barnes MMR Radiometer Spectral Bands

MMR BAND #	Central Wavelength [μm]	Inferior Wavelength [μm]	Superior Wavelength [μm]	Bandwidth (FWHM) [μm]
1	0.49	0.45	0.52	0.07
2	0.56	0.52	0.60	0.08
3	0.66	0.63	0.69	0.06
4	0.83	0.76	0.90	0.14
5	1.225	1.15	1.30	0.15
6	1.65	1.55	1.75	0.20
7	2.215	2.08	2.35	0.27
8	11.45	10.4	12.5	2.10

TABLE 2: Reflectance Uniformity Statistics

MMR BAND #	PASS #1 AVE	PASS #1 STD	PASS #1 UNCRT	PASS #2 AVE	PASS #2 STD	PASS #2 UNCRT
1	0.0297	0.0071	0.2384	0.0355	0.0104	0.2943
2	0.0209	0.0068	0.3264	0.0285	0.0110	0.3849
3	0.0139	0.0072	0.5157	0.0176	0.0104	0.5869
4	0.0136	0.0070	0.5143	0.0169	0.0108	0.6390
5	0.0138	0.0076	0.5508	0.0215	0.0129	0.5979
6	0.0145	0.0076	0.5256	0.0194	0.0116	0.6003
7	0.0139	0.0072	0.5210	0.0214	0.0114	0.5321

MMR BAND #	PASS #3 AVE	PASS #3 STD	PASS #3 UNCRT	PASS #4 AVE	PASS #4 STD	PASS #4 UNCRT
1	0.0343	0.0130	0.3795	0.0432	0.0192	0.4440
2	0.0254	0.0122	0.4815	0.0434	0.0228	0.5240
3	0.0188	0.0128	0.6819	0.0316	0.0231	0.7325
4	0.0183	0.0125	0.6837	0.0322	0.0322	1.0000
5	0.0193	0.0142	0.7367	0.0342	0.0251	0.7348
6	0.0205	0.0142	0.6934	0.0359	0.0272	0.7570
7	0.0193	0.0131	0.6799	0.0387	0.0263	0.6793

MMR BAND #	OVERALL AVE	OVERALL STD	OVERALL UNCRT
1	0.0354	0.0138	0.3891
2	0.0292	0.0165	0.5634
3	0.0203	0.0159	0.7827
4	0.0201	0.0172	0.8542
5	0.0217	0.0174	0.8011
6	0.0223	0.0184	0.8250
7	0.0231	0.0184	0.7988

NOTES: PASS #1 === 119.98 degrees West (Longitude)
PASS #2 === 120.02 degrees West (Longitude)
PASS #3 === 120.05 degrees West (Longitude)
PASS #4 === 120.08 degrees West (Longitude)

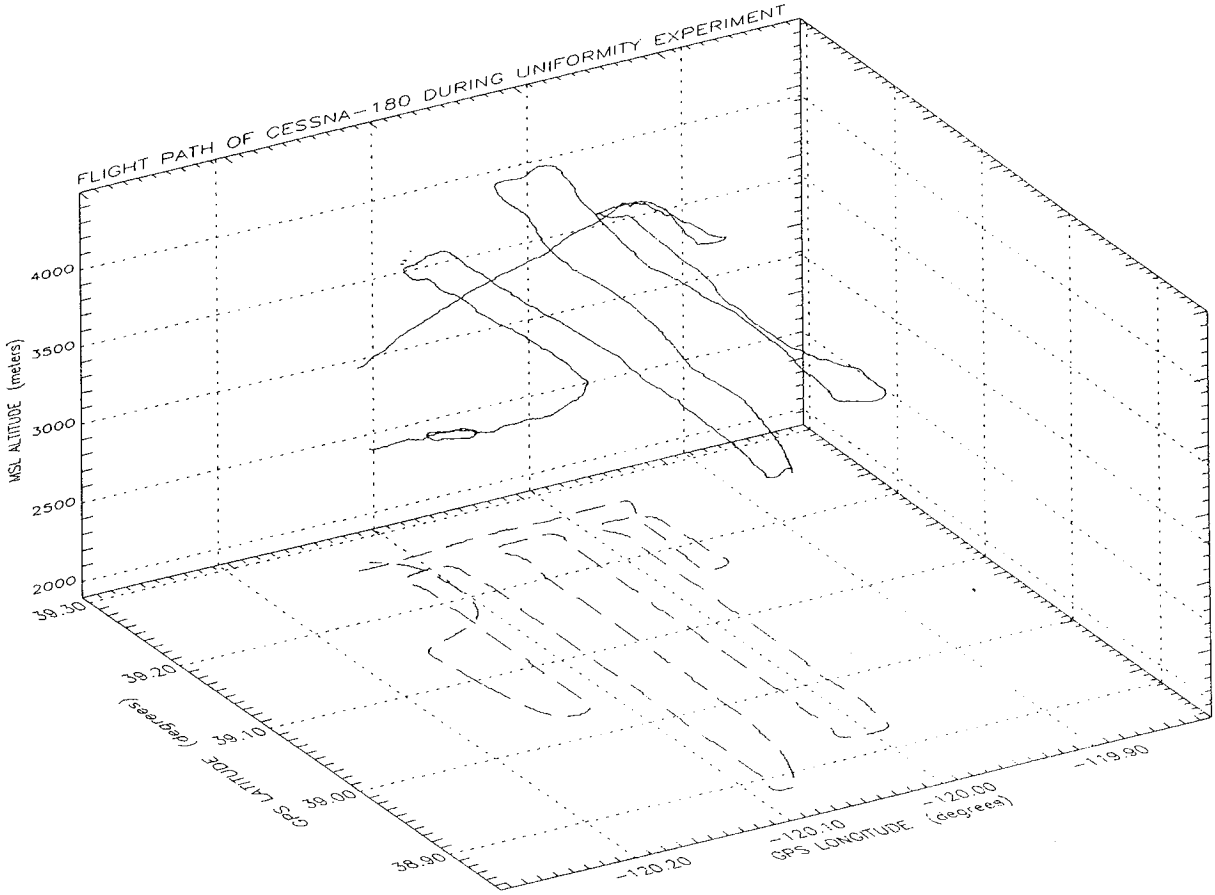
FLIGHT PATH OF CESSNA-180 DURING UNIFORMITY EXPERIMENT
MSL ALTITUDE (meters)
4000
3500
3000
2500
2000
39.30
39.20
39.10
39.00
38.90
GPS LATITUDE (degrees)
-120.20
-120.10
-120.00
-119.90
GPS LONGITUDE (degrees)

Figure 1

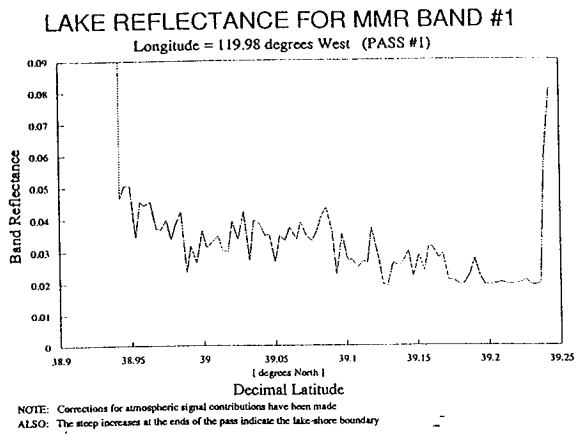

Figure 2a

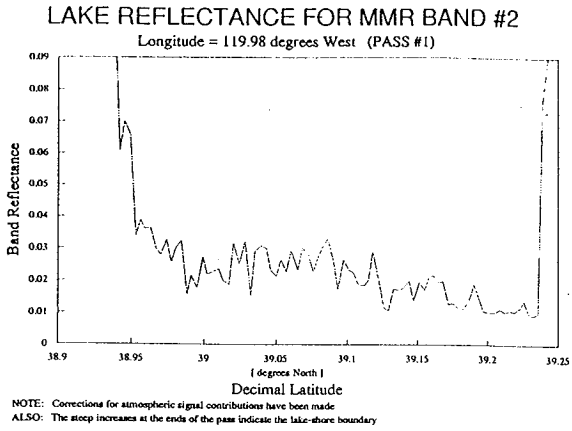

Figure 2b

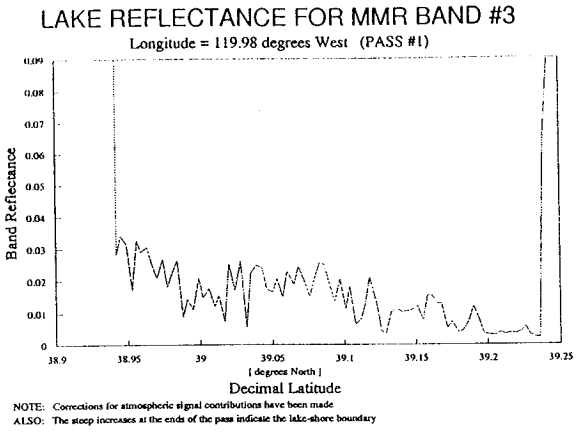

Figure 2c

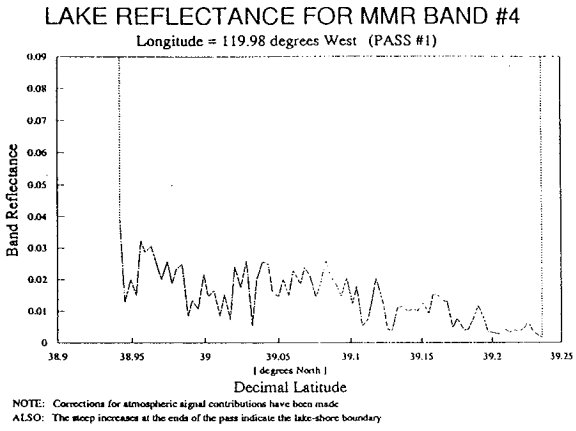

Figure 2d

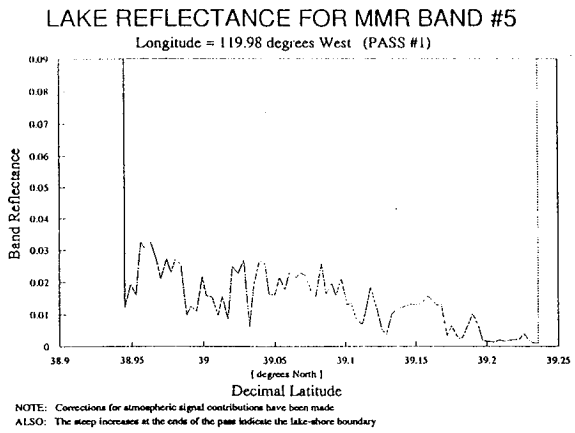

Figure 2e

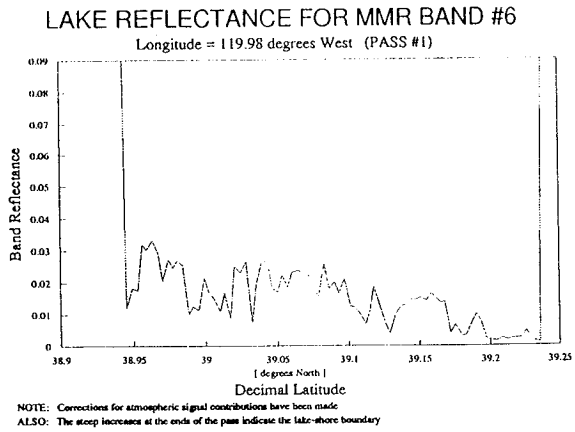

Figure 2f

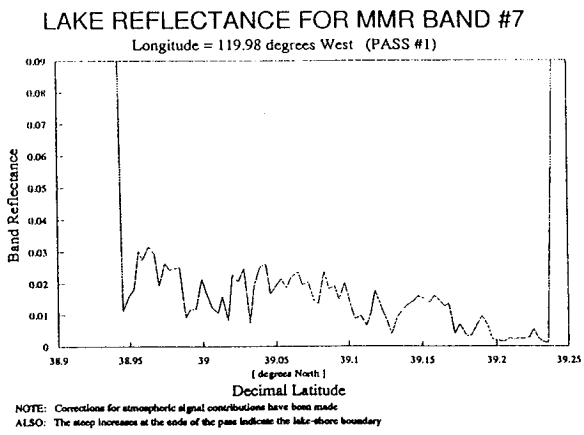

Figure 2g

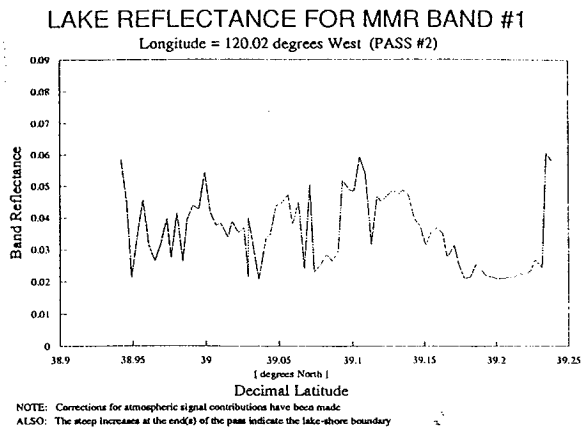

Figure 3a

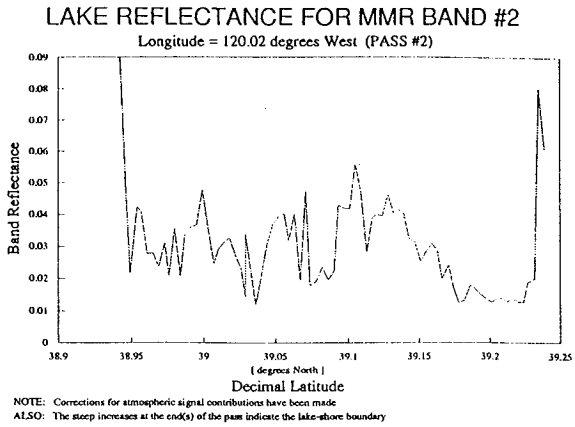

Figure 3b

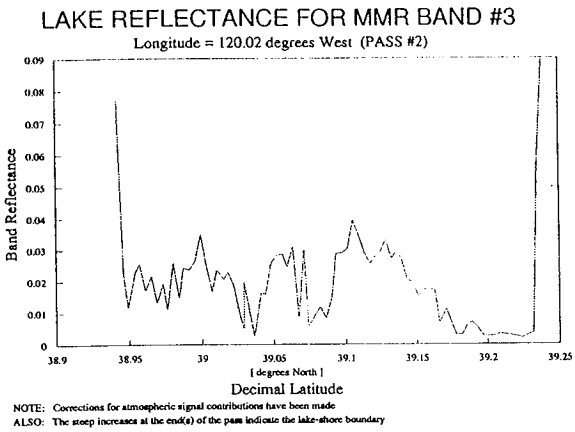

Figure 3c

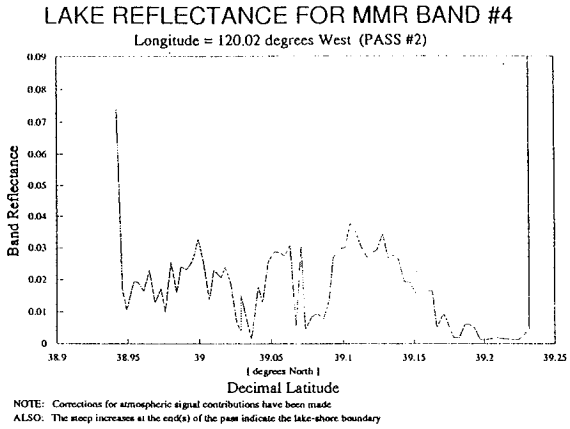

Figure 3d

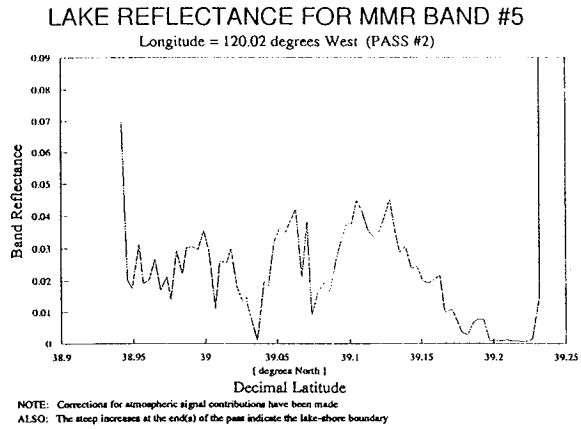

Figure 3e

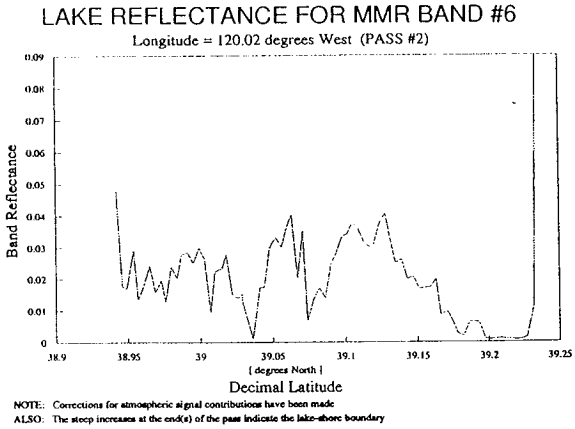

Figure 3f

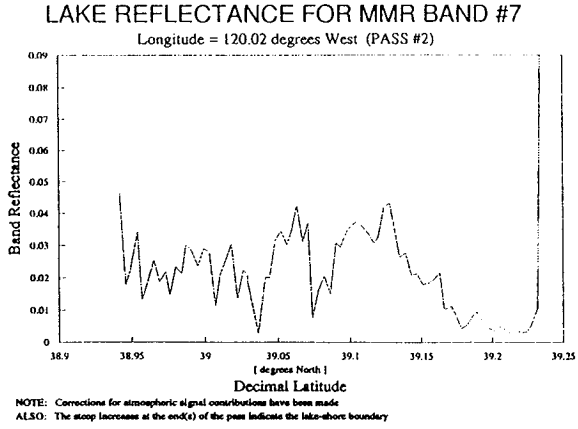

Figure 3g

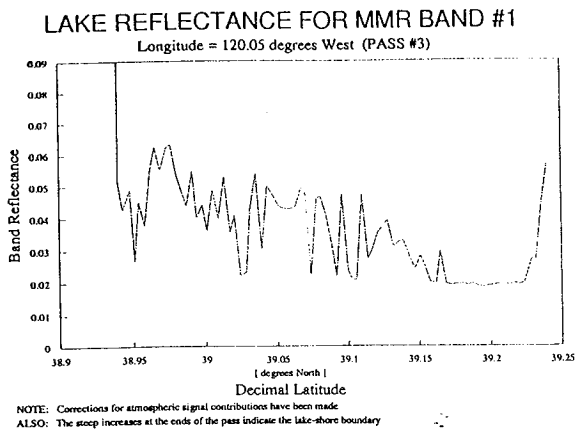

Figure 4a

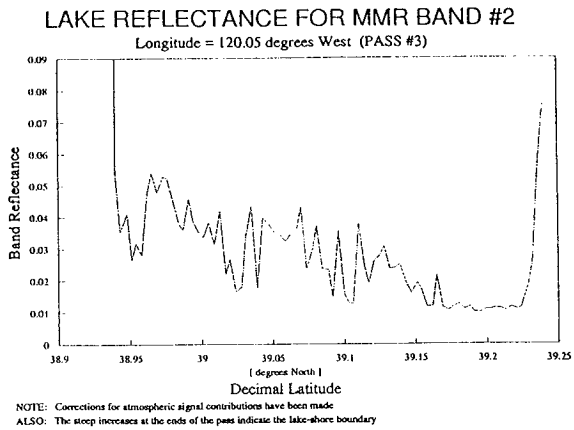

Figure 4b

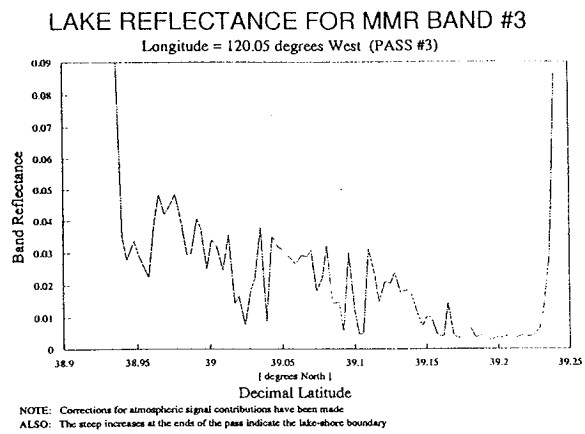

Figure 4c

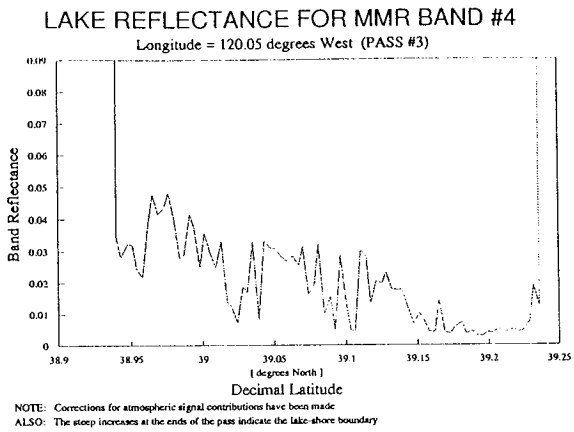

Figure 4d

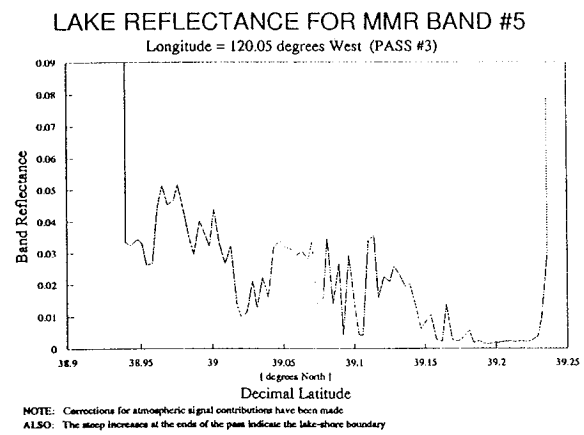

Figure 4e

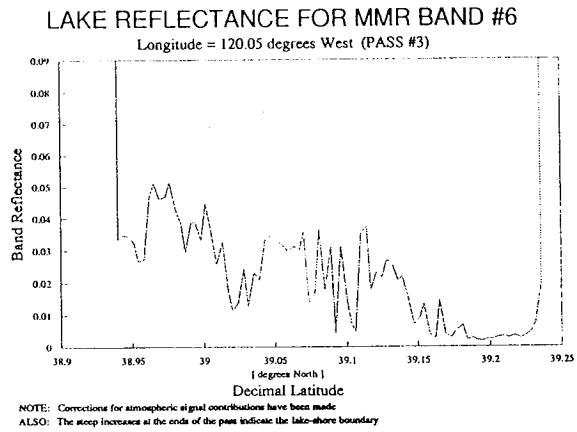

Figure 4f

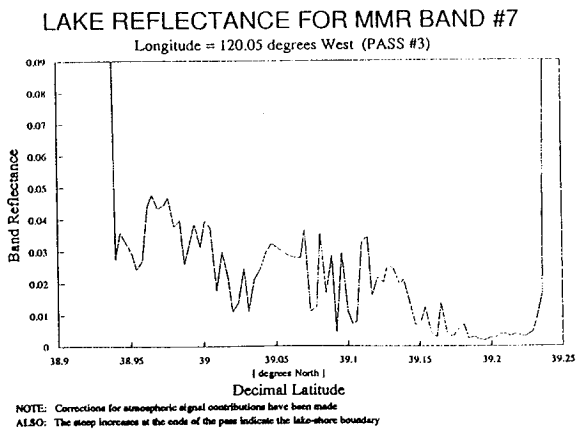

Figure 4g

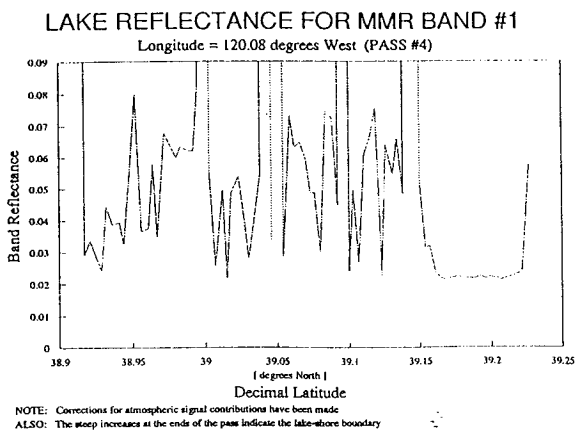

Figure 5a

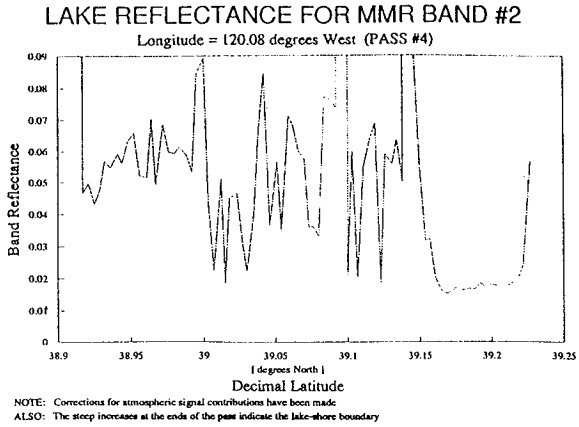

Figure 5b

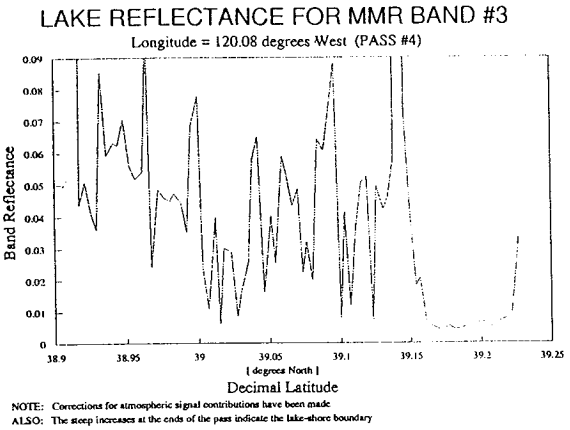

Figure 5c

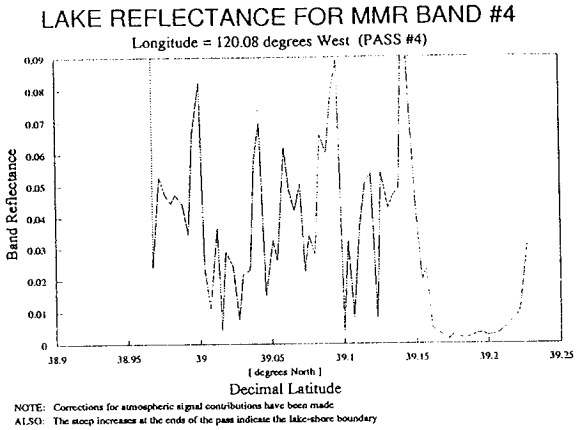

Figure 5d

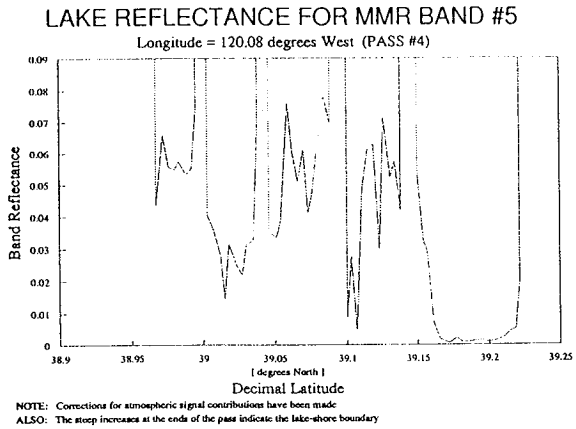

Figure 5e

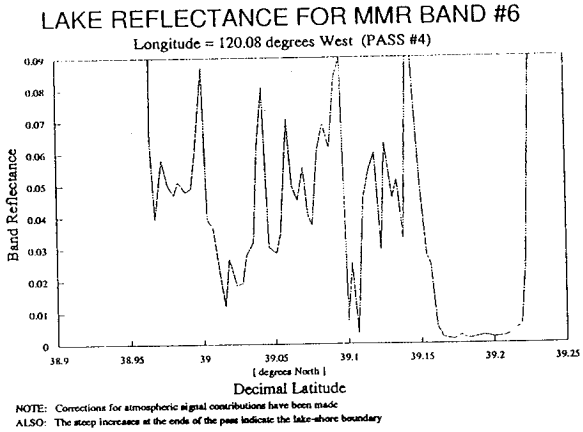

Figure 5f

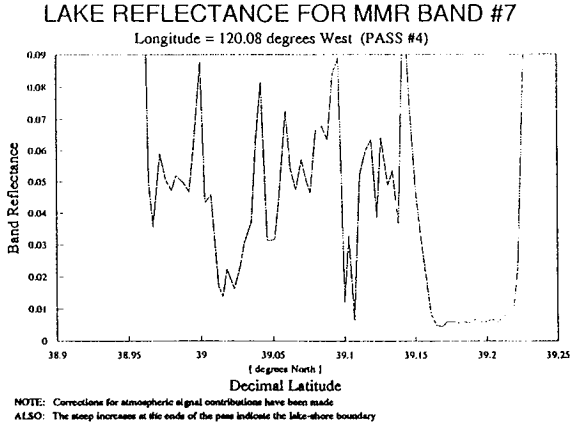

Figure 5g

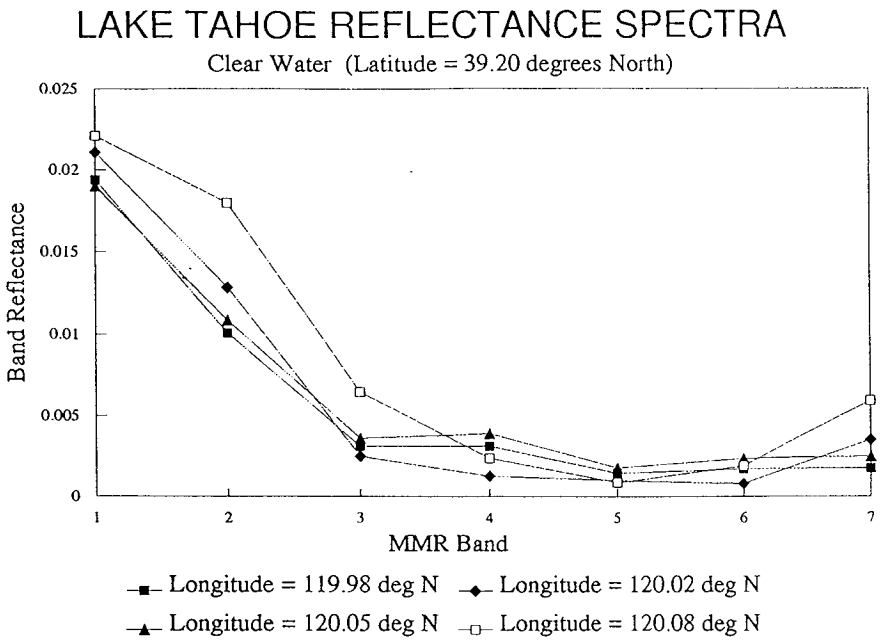

Figure 6a

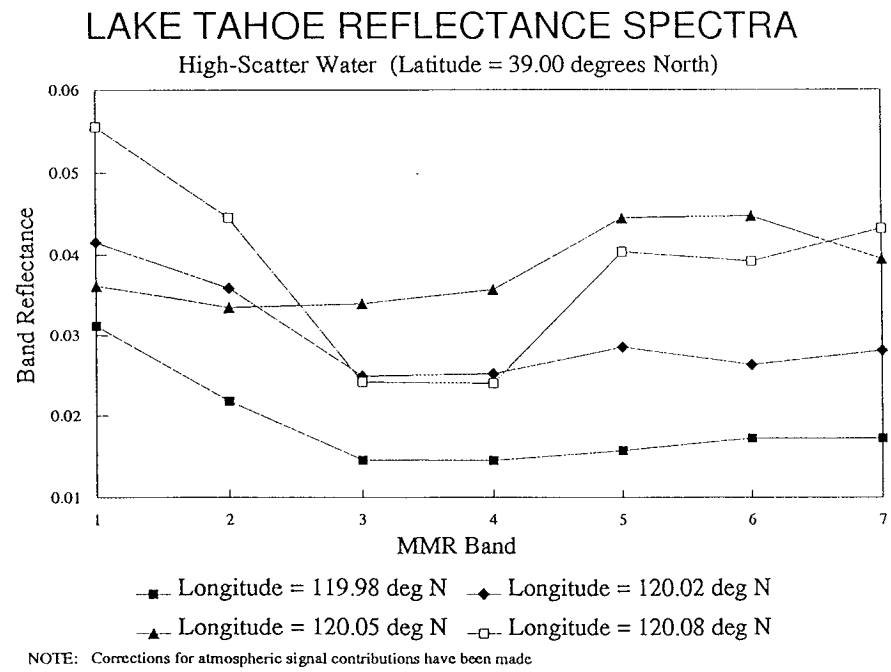

Figure 6b

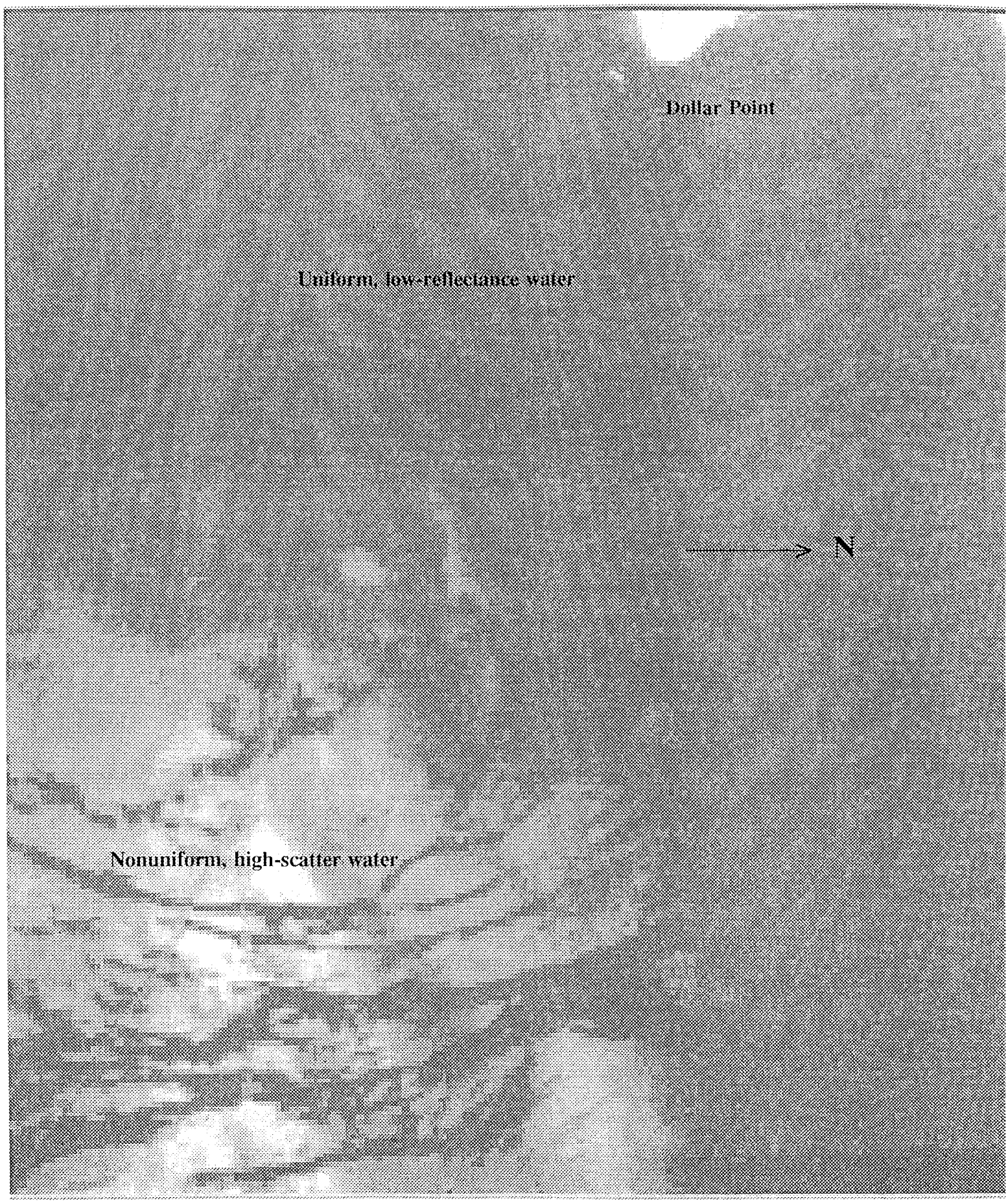

Figure 7: AVIRIS Band #31 Image of Lake Tahoe (Northern End)

On the In-Flight Vicarious Calibration of Radiometric Sensors Over Water Targets

Robert J. Parada, Jr.
Remote Sensing Group, Optical Sciences Center, University of Arizona
Tucson, Arizona 85721

Abstract

The general nature of water surfaces is discussed in relation to the problem of performing vicarious radiometric calibrations of airborne and spaceborne sensors. In addition, a brief review of two commonly employed vicarious calibration techniques, the *reflectance-based* and *radiance-based* methods, is presented and the utility of these techniques to calibrations performed over water surfaces is evaluated. It is shown that, in order for such calibration methods to be of value, certain modifications must be made due to the reflectance properties of water surfaces. Finally, a development of applicable algorithms is given. These algorithms may be used to determine the relative signal contribution of sunglint for an arbitrary solar-sensor geometry.

1.0 Introduction

The genesis of this paper resulted from a recent decision to make use of water surfaces to calibrate high-sensitivity radiometric sensors. The discussion presented is intended to familiarize the reader with the particular benefits and difficulties associated with the use of such targets for calibration purposes. In addition, a mathematical derivation of certain algorithms is presented. These algorithms have been developed to aid in determining the usefulness of an arbitrary solar-sensor geometry to the purpose of radiometric calibration by determining the effect of sunglint on the average at-sensor radiances.

The present discussion of vicarious radiometric calibration techniques is limited to the *reflectance-based* and the *radiance-based* methods. These two methods are currently employed by the Remote Sensing Group of the University of Arizona in vicarious calibrations of radiometric sensors over high-reflectance land targets.[1,2,3] A brief overview of these two techniques is given later in this paper.

Finally, the present discussion assumes that the spectral response of the intended sensor is in the solar-reflective region of the electromagnetic spectrum. This region is typically taken to include wavelengths below 2.5 μm. Vicarious calibration of sensors having a spectral response in the solar-emissive region (i.e. all longer wavelengths) is a fundamentally different problem and is not discussed herein.

2.0 Basic Properties of Water Bodies

One of the most immediately recognizable features of water bodies is their low diffuse spectral reflectance. Values close to 0.02 are typical across the entire visible range of the electromagnetic spectrum (i.e. from 0.4 μm to 0.7 μm). As a result, the contribution of the surface-reflected radiance to the total radiometric signal is small at typical sensor altitudes - which may range from tens to hundred of kilometers above ground level. This is in stark contrast to the more common land calibration targets, which typically have reflectances from 0.2 to 0.6 and have surface contributions which comprise the majority of the at-sensor signal.

In addition to the disparity in reflectance levels, water bodies differ from land calibration targets in another important way: the nature of the bi-directional reflectance distribution function (BRDF). Many land sites have BRDFs which are nearly independent of viewing direction. Such sites are therefore normally assumed to be lambertian for purposes of modeling in radiative transfer codes. Water bodies, on the other hand, are far from being lambertian. They are better classified as being specular reflectors (e.g. mirrors). Viewing direction is of critical importance since the total radiance reflected from a direction in which there is only scattered (or diffuse) radiation specularly reflected by the water is drastically different in both magnitude and spectral content from the direction in which direct solar radiation is specularly reflected by the water surface (i.e. the sunglint direction). In modeling experiments, it was determined that the apparent reflectance of a typical water body could be over 400% greater when viewing in the sunglint direction compared to viewing directions far from the glint signal.[4] This large variation occurs beyond the far-red end of the visible spectrum (λ=0.865 μm) and becomes less of a factor as wavelength decreases. The increased atmospheric scattering of shorter wavelengths contributes much more to the total sensor-level signal and thereby reduces the importance of the glint contribution.

The transparency of water at short visible wavelengths causes a small fraction of the incident radiation to be scattered back through the surface in the viewing direction. This in-water component is the property desired by oceanographers making use of the remotely sensed imagery. It comprises, at most, only a few percent of the total sensor-detected signal. The calibration uncertainties for such sensors must therefore be kept very small. (In the specific case of SeaWiFS, the uncertainty in radiometric calibration has been specified as 2-3%.)

One final, important property of water bodies is the probabilistic nature of the surface capillary wave orientations. The associated probability distribution for surface waves was deduced empirically by Cox and Munk.[5] This probability distribution is a function of both windspeed and direction, though it is similar to a rotationally symmetric Gaussian distribution for low windspeeds - making it effectively independent of wind direction. As a result of this probabilistic nature, the surface of any large water body may be thought of mathematically as being a random process. This process is stationary since the wave-slope distribution at any one location is both independent from and identical to the wave-slope distribution at another, distant point. The need to specify two points as being *distant* arises from the finite amount of

correlation between the wave-slopes at nearby points. This correlation exists both spatially and temporally. Much work concerning these correlation lengths remains to be done. At the present time the author knows of no formal work relating these correlation lengths to windspeed and direction if, indeed, such a relation exists. It is common practice to refer to each spatially correlated area as a wave 'facet'. Temporal correlation is usually not discussed or given a designation. It is an equally important property, however. As stated by Mobley, the statistical property of ergodicity applies to the wave-slope distribution.[6] This property implies that the average wave-slope measured at one point in space as a function of time will exactly match the average taken at one point in time as a function of space. Since the resultant sensor-level radiance is directly dependent on the wave-slope features of the surface, the average radiance signal can also be surmised by invoking the ergodic nature of the wave-slope distribution. These averages must be computed from independent (i.e. uncorrelated) points. Therefore, the spatial and temporal correlation lengths are of significant importance. The property of ergodicity will be shown to play a critical role in determining the utility of existing calibration techniques.

3.0 Utility of Existing Calibration Methods

Due to the particular properties of water bodies, there is a need to re-evaluate the applicability of vicarious calibration techniques traditionally applied over land surfaces to calibrations conducted over water surfaces. It is first useful to review the basic strategies underlying two specific calibration techniques: the *reflectance-based* method and the *radiance-based* method.[7,8] These two techniques are currently employed by the Remote Sensing Group of the University of Arizona to conduct vicarious radiometric calibrations of sensors over bright, nearly-lambertian land targets.

3.1 Review of calibration methods

The *reflectance-based* method of sensor calibration entails the measurement of *target reflectance* data over a calibration site during the time of sensor overpass/overflight. In addition, collection of atmospheric and meteorological data allows the inference of such parameters as Rayleigh and aerosol optical depths. These parameters are used to characterize the effect of the atmosphere on the radiometric signal collected by the sensor. The resulting data are then used in conjunction with a radiative transfer code to predict the at-sensor radiance levels. The digital counts recorded by the sensor are then compared with these radiances to produce the desired calibration coefficients.

The *radiance-based* method of sensor calibration entails the measurement of *radiance levels* at a high altitude above the target during the time of sensor overpass/overflight. These radiance levels are then corrected for the effect of the atmosphere above the sensor, which consists primarily of Rayleigh scatterers, using an appropriate radiative transfer code to obtain

the at-sensor radiance levels. In practice, measurements of the atmospheric constituents and ground reflectance are made in order to provide a check on the resulting at-sensor radiances. These radiances are compared with the sensor-recorded digital counts to produce the desired calibration coefficients.

3.2 Application of calibration methods over a water surface

Consider the utility of these two methods to calibrations performed over a bright, spatially uniform, lambertian reflector. The need to exactly duplicate the sensor angular orientation with calibration radiometers becomes unnecessary in this case due to the lambertian nature of the target. Furthermore, the uniformity of the target yields the added benefit that the measurement instruments do not need to view the exact same target area as the sensor during its overpass/overflight. These simplifications cannot be applied to highly-specular, probabilistic targets such as water bodies. For such calibration targets, the duplication of sensor viewing angles becomes a critical concern. Strictly speaking, it also becomes necessary to view the *same area* viewed by the sensor *at the very same time* as the sensor in order to insure that the signal collected by the calibration instrumentation corresponds to the radiometric signal detected by the sensor. The latter stipulations follow from the fact that a water body has an apparent reflectance that is a function both of space and of time due to the random nature of the wave-slopes present. These are rather severe constraints which must be appropriately handled/overcome in order to utilize existing calibration methods.

3.2.1 Radiance-based method

Of the two methods discussed in Section 3.1, the radiance-based method is most easily extended to the use of a water surface as the intended calibration target. However, while in practice the methodology may be identical to that when using a uniform lambertian target, the underlying theory which permits this methodology to be used is not. During calibrations involving a uniform, lambertian target the exact duplication of the sensor orientation by the calibration radiometer becomes unnecessary. For a water body, i.e. a specular target, the at-sensor radiance levels can be extremely sensitive to angular orientation. It is therefore important to exactly duplicate the sensor orientation with the flown calibration radiometer. Fortunately, this is not a serious limitation, and may be accomplished using an aircraft with appropriate mounting hardware.

Justification for applying the radiance-based method over a water target is complicated by the time-dependent nature of the radiance signal. This time-dependence is a result of the probabilistic nature of the wave-slopes. Recall that for calibrations conducted over a uniform, lambertian target, the region of the target viewed by the calibration radiometer does not need to be exactly the same as the region of the target viewed by the sensor. Furthermore, the deterministic nature of the target reflectance places a less stringent requirement on the simultaneity of the data collection. The signal contribution due to radiance reflected from a

given area of the surface is both non-uniform and a rapidly varying function of time for a water body. Strictly speaking, it then becomes critical to measure the radiance not only from the same region and the same angular orientation, but also at the same instant as the sensor. This is a practical impossibility.

There are particular circumstances in which the radiance-based method of calibration over a water surface is justified. There exist certain geometric restrictions, and the resulting calibration will always contain some element of probabilistic uncertainty due to the random nature of the target. The validity of the method is a function not only of solar-sensor geometry, but also of windspeed and the sensor field-of-view. The windspeed affects the wave-slope distribution of the surface; the sensor field-of-view defines the range of wave-slopes which may contribute a glint signal to the sensor-detected radiance. The dependence of the wave-slope distribution on windspeed is described by the Cox and Munk distribution. The effect of the sensor field-of-view requires further analysis.

Consider the extreme in which only a single wave facet lies within the sensor field-of-view at a given time. In this case, ignoring any adjacency effects, the surface contribution is dependent only on this one wave facet, which is a random variable. For such a sensor, a low level of probabilistic uncertainty in a radiance-based calibration is only obtained when the solar-sensor geometry is such that the region of sunglint lies far outside the sensor field-of-view. This implies that the probability that the facet lying within the sensor field-of view will have the appropriate wave-slope to produce a glint signal at the sensor is negligible. The signal then becomes practically independent of time - though in reality a minute level of probabilistic uncertainty still remains. Consider, however, the resolution capabilities a sensor must have to view only a single facet. A typical solar-synchronous orbital altitude is approximately 700 km. A typical capillary facet diameter of 10 cm may be assumed. A sensor viewing only one facet must consequently have an angular field-of-view of 8.19×10^{-7} degrees (or 2.95×10^{-3} arcsec). This case is therefore of little significance for most sensors.

Now, consider the opposite extreme in which many thousands of wave facets lie within the sensor field-of-view at a given time. In this case, the surface contribution is composed of contributions from each of these facets. By drawing an analogy to the law of large numbers, the sensor-detected radiance is *on average* independent of time. This is due to the relatively large number of facets which are located in a small area which subtends a differential solid angle at the sensor. At any given instant in time, approximately the same fraction of these facets will be oriented such that they produce a glint signal at the sensor. In terms of signal stability, the calibration will still be better if the solar-sensor geometry is such that the sensor field-of-view is far from the region of sunglint, or completely within this region. That is to say, when the probability of a glint-producing wave-slope is extremely small or extremely large. For small facet sizes, this extreme is the more realistic of the two discussed.

3.2.2 Reflectance-based method

The reflectance-based method is not as easily extended to the use of a water surface as the intended calibration target as is the radiance-based approach. When using a land target, the site may be spatially-sampled to obtain the mean reflectance of the surface and map out any spatial variations. Due to the temporal variability of a water surface, this is not a possibility for such sites. In addition, unlike land sites the reflectance of water surfaces must be measured at precisely the expected sensor view angle due to the specular nature of the surface.

In order to circumvent these problems, it is necessary to make use of the ergodic nature of the water surface wave-slopes. By orienting a radiometer in the viewing direction of the intended sensor and taking a measurement of surface reflectance at a given point on the water surface, the temporal average of many uncorrelated measurements should be identical to the spatial average of the surface reflectance falling within the field-of-view of a sensor. Note that this arrangement corresponds to the first extreme mentioned in Section 3.2.1 since a calibration radiometer will normally be located only a few meters above the surface of the water body so that only a few wave facets, at most, will normally lie within its field-of-view. The radiometer should have the same angular field-of-view as the intended sensor so that the same range of wave-slopes may contribute a glint signal.

The success of this "modified" reflectance-based method depends on three things: (1) in order to properly correlate these two averages, a large number of facets (as discussed in Section 3.2.1) must be present in the sensor field-of-view; (2) the sensor field-of-view must be sufficiently small so that only a small spread in wave-slopes may contribute a glint signal; (3) the temporal correlation length of the water surface's random process must be sufficiently short so that an adequate number of measurements may be taken at the approximate time of sensor overpass/over-flight to produce an adequate average. Ultimately, the utility of this method will need to be proven experimentally.

4.0 Algorithm Development

Specular reflection of direct solar radiation into the field-of-view of a sensor, or "sunglint", constitutes a much greater contribution to the sensor-detected signal than does specular reflection of diffuse skylight and from the same facet. For sensors having extremely high sensitivities, this glint signal is often sufficient to saturate the sensor and prevent calibration. The Fresnel equations determine the specular reflectance of the surface. These equations depend on the angle of incidence, Θ, and polarization of the incident radiation.

Under certain conditions, i.e. when the angular acceptance of the sensor lies far outside the primary region of sunglint, it is still possible to calibrate such high-sensitivity sensors. In fact, it is this low reflectance outside the sunglint region which makes water

surfaces such desirable calibration targets for high-sensitivity sensors. However, in certain circumstances the sensor view direction is unavoidably closer to the region of sunglint than would otherwise be desired. (For example, the Airborne Visible/Infrared Imaging Spectroradiometer, or AVIRIS, is an airborne sensor that always images in the vertically downward direction.) It is therefore important to gage the expected signal contribution from sunglint for an arbitrary solar-sensor geometry.

4.1 Determination of required facet wave-slope for given solar-sensor geometry

It is first necessary to determine the wave-slope that an arbitrary facet must have to reflect direct downward solar radiation into the sensor view direction. The geometry associated with this problem is shown in Figure 1. For this development, the water surface is assumed to be infinite, plane-parallel and to lie in the xy-plane. The z-direction is taken to be positive upward.

An incident solar ray and the associated reflected ray will each have three components. These components may be specified in terms of the x, y, and z directions. Alternatively they may be specified in terms of the angle each ray makes with respect to the z-axis, θ, and the angle made by the projection of each ray in the xy-plane to the x-axis, ϕ. An arbitrarily oriented wave-facet will have a normal which also has three components. By orienting the x-axis to be aligned with the incident solar illumination, the components of an incident ray simplify somewhat. The resulting components of the normalized incident ray are given in Equation 1.

$$\hat{i} = i_x \hat{x} + i_y \hat{y} + i_z \hat{z}$$

$$\textbf{where:} \quad i_x = -\sin\theta_s \qquad i_y = 0 \qquad i_z = -\cos\theta_s \tag{1}$$

For these components, θ_s refers to the solar zenithal angle. A normalized ray pointed in the direction of the sun will have components which are the negatives of those listed above. These components are given in Equation 2.

$$\hat{s} = s_x \hat{x} + s_y \hat{y} + s_z \hat{z}$$

$$\textbf{where:} \quad s_x = \sin\theta_s \qquad s_y = 0 \qquad s_z = \cos\theta_s \tag{2}$$

The components for a normalized reflected ray are given in Equation 3.

$$\hat{r} = r_x \hat{x} + r_y \hat{y} + r_z \hat{z}$$

$$\textbf{where:} \quad r_x = \sin\theta_v \cos\Delta\phi \qquad r_y = \sin\theta_v \sin\Delta\phi \qquad r_z = \cos\theta_v \tag{3}$$

For these components, θ_v refers to the view zenithal angle and $\Delta\phi$ refers to the relative azimuthal difference of the sensor view direction with respect to the solar illumination direction. In addition to these rays, the orientation of an arbitrary wave facet may also be specified in terms of three components. The components of the normal for an arbitrary wave facet are given in Equation 4. In this set of equations, θ_f refers to the facet normal zenithal angle and ϕ_f refers to the facet azimuthal angle as measured from the x-axis (i.e. relative to the solar azimuth).

$$\hat{n} = n_x \hat{x} + n_y \hat{y} + n_z \hat{z}$$

$$\textbf{where:} \quad n_x = \sin\theta_f \cos\phi_f \qquad n_y = \sin\theta_f \sin\phi_f \qquad n_z = \cos\theta_f \tag{4}$$

Making use of these vector relationships, and by applying the Law of Reflection to each component, the facet angles (θ_f, ϕ_f) needed to reflect the incident solar illumination in the viewing direction of the sensor may be determined. This line of development has been followed in the past by Cox and Munk.[5] The resulting component equations are shown below:

$$
\begin{aligned}
r_x - i_x &= r_x + s_x = n_x(2\cos\Theta) \\
r_y - i_y &= r_y + s_y = n_y(2\cos\Theta) \\
r_z - i_z &= r_z + s_z = n_z(2\cos\Theta).
\end{aligned} \tag{5}
$$

These equations show that the difference between the incident and (specularly) reflected ray components will be proportional to the respective facet normal component. In this set of equations, Θ is the angle bisecting the solar and reflected rays, $\cos\Theta$ is a factor of proportionality, and the factor of two arises due to the difference taken between the incident and reflected components. Note that there are now three equations, but four unknowns: n_x, n_y, n_z, and Θ. By squaring and adding all three relations from Equation 5, and noting that $n_x^2 + n_y^2 + n_z^2 = 1$, an additional relationship is obtained:

$$
\cos^2\Theta = \frac{1}{2}[1 + \cos\theta_s\cos\theta_v + \sin\theta_s\sin\theta_v\cos\Delta\phi]. \tag{6}
$$

These four relationships permit the determination of the facet normal components required to reflect incident solar illumination into the viewing direction of the sensor. The resulting relations, obtained after solving the set of linear relations given in equations 5 and 6, are given in Equations 7.

$$
\begin{aligned}
\theta_f &= \cos^{-1}\left(\frac{\cos\theta_v + \cos\theta_s}{2\cos\Theta}\right) \\
\phi_f &= \sin^{-1}\left(\frac{\sin\theta_s\sin\Delta\phi}{2\sin\theta_f\cos\Theta}\right)
\end{aligned} \tag{7}
$$

Note that these relations depend completely on a given solar-sensor geometry. They may be re-written to provide information concerning the wave-slope components of the facet. The relationships between wave-slope components and the facet orientation angles are given in Equations 8.

$$z_x = \frac{\partial f}{\partial x} = \tan\theta_f \cos\phi_f$$
$$z_y = \frac{\partial f}{\partial y} = \tan\theta_f \sin\phi_f \qquad (8)$$

In these relations, f = f(x,y) represents the (planar) facet surface height function. Through these equations, the probability of the required wave-slope facet being present may be determined based on the Cox and Munk (or other appropriate) probability distribution. This is discussed more fully in Section 4.4.

4.2 Determination of associated interface reflectance

Once the angle of incidence, Θ, has been determined from Equation 6, the fraction of incident solar illumination reflected by the facet may be determined using the Fresnel relations. This development has been carried out in the literature by Cracknell.[9] The resulting reflectance expressions are given in Equation 9.

$$R(\Theta,\lambda) = \rho_{H\perp}^{\,2}(\Theta,\lambda) + \rho_{E\perp}^{\,2}(\Theta,\lambda)$$

$$\textbf{\textit{where:}}\quad \rho_{H\perp}(\Theta,\lambda) = \frac{\sqrt{n^2(\lambda) - \sin^2\Theta} - n^2(\lambda)\cos\Theta}{\sqrt{n^2(\lambda) - \sin^2\Theta} + n^2(\lambda)\cos\Theta} \qquad (9)$$

$$\rho_{E\perp}(\Theta,\lambda) = \frac{\cos\Theta - \sqrt{n^2(\lambda) - \sin^2\Theta}}{\cos\Theta + \sqrt{n^2(\lambda) - \sin^2\Theta}}$$

In this group of equations, $\rho_{H\perp}(\Theta,\lambda)$ represents the amplitude reflection coefficient for the transverse magnetic component of the incident solar wave and $\rho_{E\perp}(\Theta,\lambda)$ represents the amplitude reflection coefficient for the transverse electric component of the incident solar wave. Note that the wavelength dependence of these coefficients has been written explicitly. Using these relations, the reflectance, $R(\Theta,\lambda)$, can be determined for each wave facet within the sensor field-of-view.

4.3 Handling of sensor field-of-view

Due to the finite size of the instantaneous field-of-view which any sensor possesses, a

range of wave-slopes are actually capable of giving rise to a glint contribution in the at-sensor radiance. This range of wave-slopes will be dependent on both the solar-sensor geometry and the sensor instantaneous field-of-view. Therefore, the need arises to properly handle this range of wave-slopes. In order to accomplish this, a closer look must be taken at the general sensor view geometry - including field-of-view.

The associated geometry of an arbitrary sensor is shown in Figures 2 through 5. Each of these figures presents a point of view used in the derivation of spatial and angular relationships for the sensor. Figure 2a shows a zenithal cross-section of the sensor field-of-view for a vertically downward view direction; Figure 2b shows the same cross-section for some non-vertical view angle, $\theta_o \neq 0$. Figure 3 shows an azimuthal cross-section of the sensor field-of-view for this same non-vertical view direction. Note that the instantaneous field-of-view forms an elliptical footprint. Figure 4 illustrates how the view direction changes depending on the position of a point within the instantaneous sensor field-of-view. Figure 5 illustrates how the view azimuthal angle changes depending on the position of a point within the instantaneous field-of-view. Each of these figures will be discussed in more detail during the course of the ensuing development.

Consider, first, the simplest sensor view geometry: a vertically downward view direction. In this case, the instantaneous field-of-view is symmetric about the vertical direction and the ground footprint is circular. This situation is depicted in Figure 2a. The simple relation connecting the sensor altitude, h, the footprint radius , r, and the field-of-view angular half-width, δ_θ, is shown below:

$$r = h\tan\delta_\theta . \tag{10}$$

The case of a non-vertical view angle must reduce to this simple relationship as the view angle approaches the vertical direction. This more general geometry is illustrated in Figure 2b. In this figure, line segment BC represents the extent of the sensor footprint on the target while point O represents the sub-sensor point. The sensor view zenithal angle is designated by θ_o, while the field-of-view angular half-width is again designated by δ_θ. The length from the sensor to the point at the center of the field-of-view is designated by d = DA, while the lateral distance from the sub-sensor point to the point at which a ray directed along the center of the sensor field-of-view intersects the sensor footprint is designated by x_o = OA. Relationships between these latter two quantities and the viewing geometry of the sensor are shown in Equations 11.

$$\begin{aligned} d &= h\sec\theta_o \\ x_o &= h\tan\theta_o \end{aligned} \tag{11}$$

An additional relation is obtained by constructing an equilateral triangle such that point A lies at the center of the base, which has a length of $2b_o$, as shown:

$$b_o = d\tan\delta_\theta = h\left(\frac{\tan\delta_\theta}{\cos\theta_o}\right). \tag{12}$$

This relation is needed to develop expressions for the two line segments comprising the length of the sensor footprint, x_1 and x_2. The length x_1 may be written in terms of b_o by making use of an oblique triangle mensuration formula (otherwise known as the Law of Sines), as shown in Equation 13.

$$\frac{x_1}{b_o} = \frac{\sin\mu}{\sin(\pi-\alpha)}$$

$$\textit{But:} \quad \sin\mu = \cos\delta_\theta \qquad \sin(\pi-\alpha) = \cos(\theta_o - \delta_\theta) \tag{13}$$

$$\textit{Substitution yields:} \quad x_1 = b_o\left(\frac{\cos\delta_\theta}{\cos(\theta_o - \delta_\theta)}\right)$$

A similar expression for x_2 is shown in Equation 14.

$$\frac{x_2}{b_o} = \frac{\sin\eta}{\sin\beta}$$

$$\textit{But:} \quad \sin\eta = \cos\delta_\theta \qquad \sin\beta = \cos(\theta_o + \delta_\theta) \tag{14}$$

$$\textit{Substitution yields:} \quad x_2 = b_o\left(\frac{\cos\delta_\theta}{\cos(\theta_o + \delta_\theta)}\right)$$

It is worth noting that, as expected, when $\theta_o = 0$ then $x_1 = x_2 = b_o = r$ from Figure 1 so that these results are consistent with the case of a vertical downward view direction.

Having determined relationships for x_1 and x_2, expressions for the semi-major axis, a, and semi-minor axis, b, of the sensor's elliptical footprint may now be developed. An illustration of this ellipse is shown in Figure 3. The relationship connecting the former two quantities to the semi-major axis is straightforward and is presented below:

$$a = \frac{x_1 + x_2}{2}. \tag{15}$$

The relation for the semi-minor axis is more complex, and makes use of equilateral triangle ΔDEF shown in Figure 2b. When this triangle is rotated about the ray at the middle of the sensor's angular field-of-view, the figure of revolution produced is a right-circular cone. Point P in Figure 3 is the location at which this cone intersects the elliptical footprint, and the length of the shortest line connecting the semi-major axis to this point is simply b_o. The general expression for the ellipse is shown in Equation 16.

$$\frac{(x_v - x_c)^2}{a^2} + \frac{y_v^2}{b^2} = 1 \tag{16}$$

The coordinate system of this ellipse has been specified with the origin lying at the sub-sensor point and the axis aligned along the semi-major and semi-minor axes of the ellipse. This convention is illustrated in Figure 4. Note that the center of the ellipse $(x_c, 0)$ and the point at which a ray directed along the center of the sensor field-of-view intersects the sensor footprint $(x_o, 0)$ are not synonymous unless $\theta_o = 0$. The derivation of an expression for the semi-minor axis is given in Appendix A. The resulting relation is given below:

$$b = \frac{h}{2}\sqrt{\frac{x_1}{x_2}\left(1 + \frac{x_2}{x_1}\right)\left(\frac{\tan\delta_\theta}{\cos\theta_o}\right)}. \tag{17}$$

The elliptical footprint of the sensor has now been fully characterized and may be used to determine the exact view zenithal and azimuthal angles of each point bordering (and within) this area. As can be seen from Figure 2b, the maximum and minimum values of x_v are:

$$x_v^{max} = h\tan(\theta_o + \delta_\theta)$$
$$x_v^{min} = h\tan(\theta_o - \delta_\theta). \quad (18)$$

For this range of values, the equation of the ellipse may be used to determine the corresponding values of y_v for the points on the border of the sensor footprint. After inverting the ellipse equation, the result shown in Equation 19 is obtained.

$$y_v = \pm b\sqrt{1-\left(\frac{x_v - x_c}{a}\right)^2} \quad (19)$$

For a given coordinate pair (x_p, y_p), the zenithal and azimuthal angles may then be computed as shown below:

$$\theta_p = \tan^{-1}\left(\frac{\sqrt{x_p^2 + y_p^2}}{h}\right)$$
$$\Delta\phi_p = \Delta\phi + \tan^{-1}\left(\frac{y_p}{x_p}\right). \quad (20)$$

The subscript p refers to the fact that these quantities are dependent on the location of a given point within the sensor footprint. Note that the azimuthal angle has been corrected so that it is properly rotated back into the coordinate system defined by the incident solar ray. An illustration of the relation between these two coordinate systems is shown in Figure 5. The associated proof of this coordinate rotation in given in Appendix B.

4.4 Determination of the glint contribution to the at-sensor signal

Now that the view direction for each point within the sensor footprint is known, the wave-slope facet required to reflect the incident solar illumination into the sensor field-of-view may be calculated by applying of the expressions developed in Section 4.1. The reflectance coefficient for each wave-slope may then be computed by using the relations presented in Section 4.2, and the corresponding probability of such a wave-slope may be

determined from the Cox and Munk (or other appropriate) distribution. These steps will permit the determination of the average contribution of sunglint to the at-sensor signal for an arbitrary solar-sensor geometry.

As any realistic determination of the glint contribution will involve a numerical method of solution, it is necessary to discuss how the probability of a given wave-slope may be determined. For an arbitrary wave-slope probability distribution function, $p(z_x, z_y)$, the associated probability that a facet has a wave-slope components (z_{xo}, z_{yo}) within some tolerance $(\delta z_x, \delta z_y)$ is given by the following expression:

$$P(z_{xo}, z_{yo}) = p(z_{xo}, z_{yo})\, \delta z_x\, \delta z_y . \tag{21}$$

Cox and Munk developed the associated two-dimensional tolerance in terms of a tolerance ellipse of area $\Delta_t(z_{xo}, z_{yo})$.[5] This ellipse is centered about the point (z_{xo}, z_{yo}) in wave-slope space and results from the finite angular subtense of the sun at the water surface. The corresponding expression for the tolerance ellipse is shown in Equation 22.

$$\Delta_t(z_{xo}, z_{yo}) = \frac{1}{4}\pi\epsilon^2 \sec^3\theta_f \sec\Theta \tag{22}$$

In the above expression, $2\epsilon = 32.0'$ is the angular diameter of the sun. Using the established notation, θ_f is the zenithal angle of the facet normal (which, for a particular location within the sensor footprint, may also be written θ_p) and Θ is the associated angle of incidence/reflection for the facet.

Having developed an expression for the probability of a given wave-slope, we now seek to extend the result to the entire field-of-view, and therefore to determine the total glint contribution to the at-sensor radiance. In order to accomplish this, a certain amount of information about the magnitude of the direct and diffuse solar illumination incident on the water surface is required. In addition, knowledge of the in-water reflectance for the water body is required.

For the sake of simplicity, the diffuse component of the downward radiance is assumed to be independent of direction so that anisotropic scattering, polarization effects, and path-dependent optical attenuation are all ignored. The resulting model then reduces to a binary illumination condition for the purposes of Fresnel reflectance from the water surface: the direct solar radiance, L_λ^{dir}, is used for waves having the appropriate slope to produce a glint signal at the sensor; the diffuse solar radiance, L_λ^{dif}, is used for all other waves. The corresponding *average* water-leaving glint contribution becomes:

$$L_\lambda^{glint} = R(\Theta,\lambda)\, P(z_{xo}, z_{yo})\, L_\lambda^{dir}. \tag{23}$$

Similarly, the corresponding *average* water-leaving (diffuse) skylight contribution becomes:

$$L_\lambda^{sky} = \langle R(\Theta,\lambda) \rangle [1 - P(z_{xo}, z_{yo})]\, L_\lambda^{dif}. \tag{24}$$

In this expression, the angled brackets indicate an average reflectance coefficient for all possible angles from which diffuse solar radiance may be incident.

The in-water reflectance is assumed to be lambertian in nature. For this reason, the total downward irradiance, E_λ^{tot}, is needed to determine the associated in-water signal contribution. The corresponding water-leaving signal contribution becomes:

$$L_\lambda^{wat} = R_{wat}(\lambda)\, E_\lambda^{tot}. \tag{25}$$

In this expression, $R_{wat}(\lambda)$ represents the spectral in-water reflectance coefficient.

Finally, the relative importance of these three components may be computed as shown in Equations 26.

$$\begin{aligned}
\textit{glint fraction} &= \frac{L_\lambda^{glint}}{L_\lambda^{glint} + L_\lambda^{sky} + L_\lambda^{wat}} \\
\textit{skylight fraction} &= \frac{L_\lambda^{sky}}{L_\lambda^{glint} + L_\lambda^{sky} + L_\lambda^{wat}} \\
\textit{inwater fraction} &= \frac{L_\lambda^{wat}}{L_\lambda^{glint} + L_\lambda^{sky} + L_\lambda^{wat}}
\end{aligned} \tag{26}$$

5.0 Conclusions

This paper has been meant to impart an understanding of the concerns and difficulties unique to the problem of using a water surface as a calibration target. An explanation of the basic properties of water bodies has been given along with a discussion of how existing calibration methods may be effectively used over such targets. Finally, a derivation of algorithms useful to the purpose of determining the effects of sunglint for an arbitrary solar-sensor geometry has been presented.

It is apparent that calibrations over water bodies involve a higher degree of complexity both in theory and in practice than do calibrations conducted over land sites. The primary advantage gained by using a water surface as a calibration target is the ability to calibrate sensors having extremely high sensitivities. Under certain circumstances, a great number of the difficulties and uncertainties associated with over-water calibrations may be minimized. It is hoped that in the near future experimental data resulting from such calibrations will be available for analysis and further refinement of the modifications required when employing established calibration methods.

Appendix A: Derivation of Semi-Minor Axis Expression

As seen in Figures 3 and 4, the sensor footprint ellipse is centered about the point $(x_c, 0)$. The shift of this center along the x_v axis is given by the relation in Equation A1.

$$x_c = x_o - x_1 + a = x_o + \frac{x_2 - x_1}{2} \qquad \textbf{(A1)}$$

$$\textit{Since:} \quad 2a = x_1 + x_2$$

The equation of this ellipse was presented previously as Equation 16 and is restated below:

$$\frac{(x_v - x_c)^2}{a^2} + \frac{y_v^2}{b^2} = 1. \qquad \textbf{(A2)}$$

As discussed in Section 4.3 and shown in Figure 3, the length of the line connecting point P on the ellipse to the semi-major axis at point A is simply b_o. For point P in the above ellipse equation, $(x_v - x_c) = \pm(a - x_1)$ and $y_v = \pm b_o$. Using this known solution, the ellipse equation may be inverted to obtain an expression for b. This is shown in Equations A3.

$$\frac{(a - x_1)^2}{a^2} + \frac{b_o^2}{b^2} = \left(1 - \frac{x_1}{a}\right)^2 + \frac{b_o^2}{b^2} = 1$$

$$\textit{Solving for } b\text{:} \quad b = \frac{b_o}{\sqrt{1 - \left(1 - \frac{x_1}{a}\right)^2}}. \tag{A3}$$

After further algebraic simplification, this relation reduces to that presented in Section 4.3 as Equation 17. This relation has been restated as Equation A4.

$$b = \frac{h}{2}\sqrt{\frac{x_1}{x_2}}\left(1 + \frac{x_2}{x_1}\right)\left(\frac{\tan\delta_\theta}{\cos\theta_o}\right) \tag{A4}$$

Appendix B: Justification of Azimuthal Coordinate Rotation

The geometry associated with this development is illustrated in Figure 5 which represents the projection of the solar ray, the sensor view ray, and the sensor field-of-view onto the target surface. As depicted in this figure, the angular relations given below hold:

$$\alpha = \pi - (\Delta\phi + \delta_\phi)$$

$$\Delta\phi_p = \pi - \alpha \tag{B1}$$

$$\therefore \quad \Delta\phi_p = \Delta\phi + \delta_\phi.$$

In addition, by noting the relationship between δ_ϕ and the point coordinates (x_p,y_p), this expression may be rewritten as shown in Equation B2.

$$\delta_{\phi} = \tan^{-1}\left(\frac{y_p}{x_p}\right)$$

$$\therefore \quad \Delta\phi_p = \Delta\phi + \tan^{-1}\left(\frac{y_p}{x_p}\right) \qquad \textbf{(B2)}$$

References

1. Thome, K.J., D.I. Gellman, R.J. Parada, S.F. Biggar, P.N. Slater, and M.S. Moran, 1993: In-flight radiometric calibration of Landsat-5 Thematic Mapper from 1984 to present, *Proc. SPIE*, **1938**(14): 126-130.

2. Gellman, D.I., S.F. Biggar, M.C. Dinguirard, P.J. Henry, M.S. Moran, K.J. Thome, and P.N. Slater, 1993: Review of SPOT-1 and -2 calibrations at White Sands from launch to the present, *Proc. SPIE.*, **1938**(13): 118-125.

3. Balick, L.K., C.J. Golanics, J.E. Shines, S.F. Biggar, and P.N. Slater, 1991: The in-flight calibration of a helicopter-mounted Daedalus multispectral scanner, *Proc. SPIE*, **1493**: 215-223.

4. Parada, R.J., and R. Santer, 1993: *An overview of radiative transfer codes for the vicarious calibration of SeaWiFS*, Remote Sensing Group of the Optical Sciences Center, University of Arizona, Tucson Arizona, 85721, 24pp.

5. Cox, C., and W. Munk, 1954: Measurement of the roughness of the sea surface from photographs of the Sun's glitter, *Journal of the Optical Society of America*, **44**: 838-850.

6. Mobley, C.D., 1994: *Light and Water: Radiative Transfer in Natural Waters*, Academic Press, Inc., San Diego, p. 168.

7. Slater, P.N., S.F. Biggar, R.G. Holm, R.D. Jackson, Y. Mao, M.S. Moran, J.M. Palmer, and B. Yuan, 1987: Reflectance- and radiance-based methods for the in-flight absolute calibration of multispectral sensors, *Remot. Sens. Environ.*, **22**: 11-37.

8. Slater, P.N., S.F. Biggar, K.J. Thome, D.I. Gellman, and P.R. Spyak, 1995: Vicarious radiometric calibrations of EOS sensors, *Journal of Atmospheric and Oceanic Technology*, in press.

9. Cracknell, A.P., 1993: A method for the correction of sea surface temperatures derived from satellite thermal infrared data in an area of sunglint, *Int. J. Remote Sensing*, **14**(1): 3-8.

FIGURE CAPTIONS

Figure 1. An illustration of the geometry associated with an arbitrary wave facet. Note that the x-axis is taken to lie along the solar azimuth. The view azimuth (i.e. the direction of reflection) is measured relative to this axis. In addition to the (normalized) solar and reflected rays, the facet normal is shown.

Figure 2a. The zenithal cross-section of field-of-view for a sensor viewing in the downward vertical direction (i.e. with view zenithal angle $\theta_o = 0$). The sensor is located at an altitude of h above the calibration target and has a field-of-view angular half-width of δ_θ.

Figure 2b. The zenithal cross-section of the field-of-view for a sensor viewing at zenithal angle θ_o. The sensor is located at an altitude of h above the calibration target and has a field-of-view angular half-width of δ_θ.

Figure 3. The azimuthal cross-section of the field-of-view for a sensor viewing at zenithal angle θ_o. The sensor footprint is elliptical and is shifted from the sub-sensor point by distance x_c. Point P is intimately related to isosceles triangle ΔDEF depicted in Figure 2b. The coordinate system shown corresponds to the sensor footprint rather than to the present solar geometry.

Figure 4. An illustration showing sensor field-of-view for a general sensor view geometry. Note how the precise view direction (θ_p,ϕ_p) changes depending on the position of a point within the instantaneous field-of-view of the sensor. The coordinate system shown corresponds to the sensor footprint rather than to the present solar geometry.

Figure 5. An illustration of the relation between the global (i.e. solar-geometry-based) and local (i.e. sensor-footprint-based) coordinate. The included lines represent the projections of the solar ray and the precise sensor view ray (for a given point on the boundary of the sensor footprint) onto the target plane. This picture depicts how the local azimuthal angle may be corrected so that it is properly rotated back into the global coordinate system.

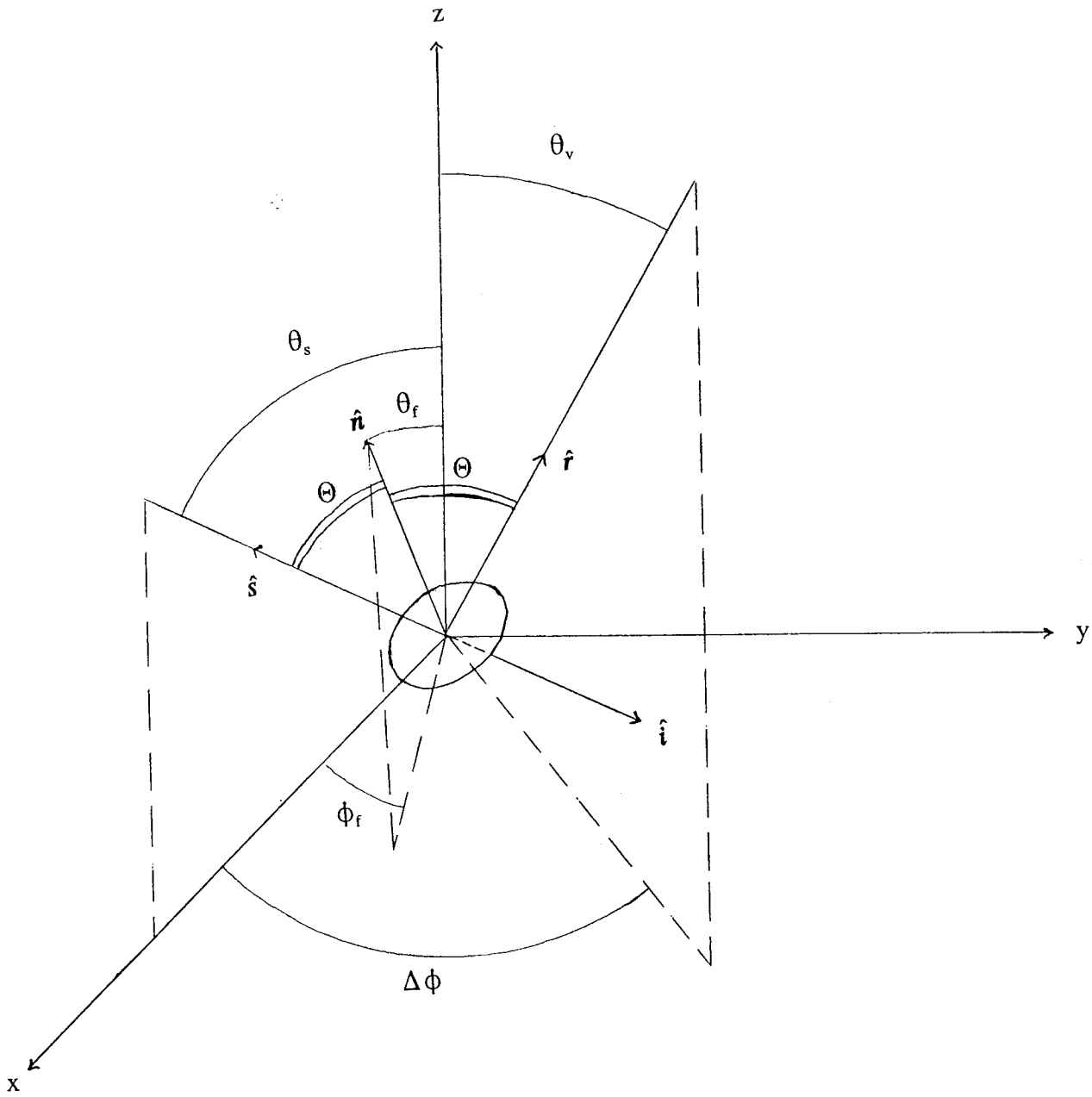
z
θ_v
θ_s
θ_f
$\hat{n}$
Θ
Θ
$\hat{r}$
$\hat{s}$
y
$\hat{i}$
ϕ_f
$\Delta\phi$
x

Figure 1

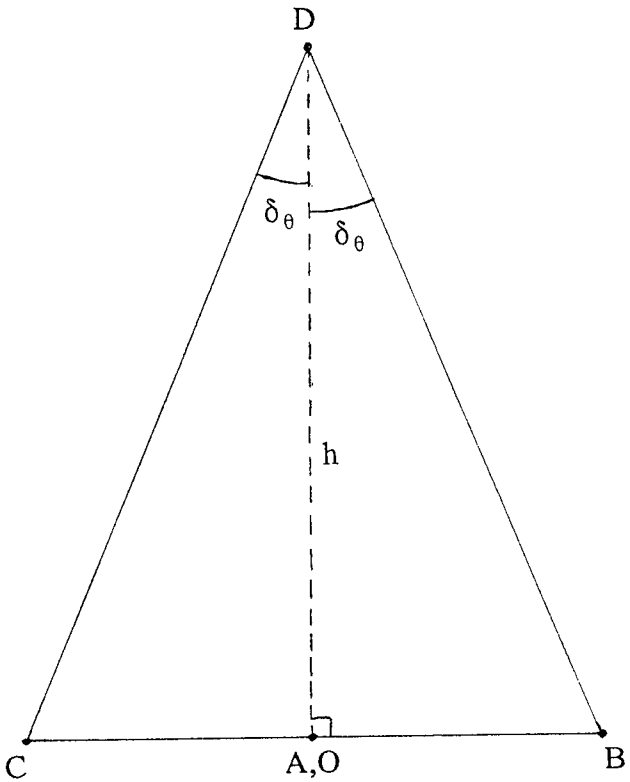

Figure 2a

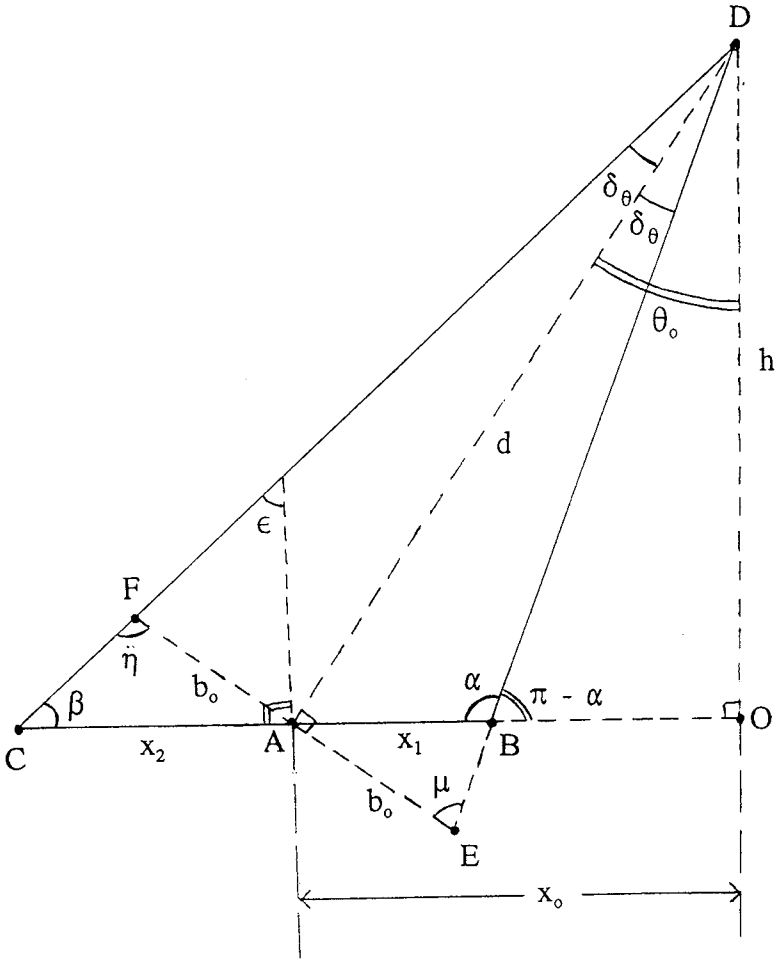

Figure 2b

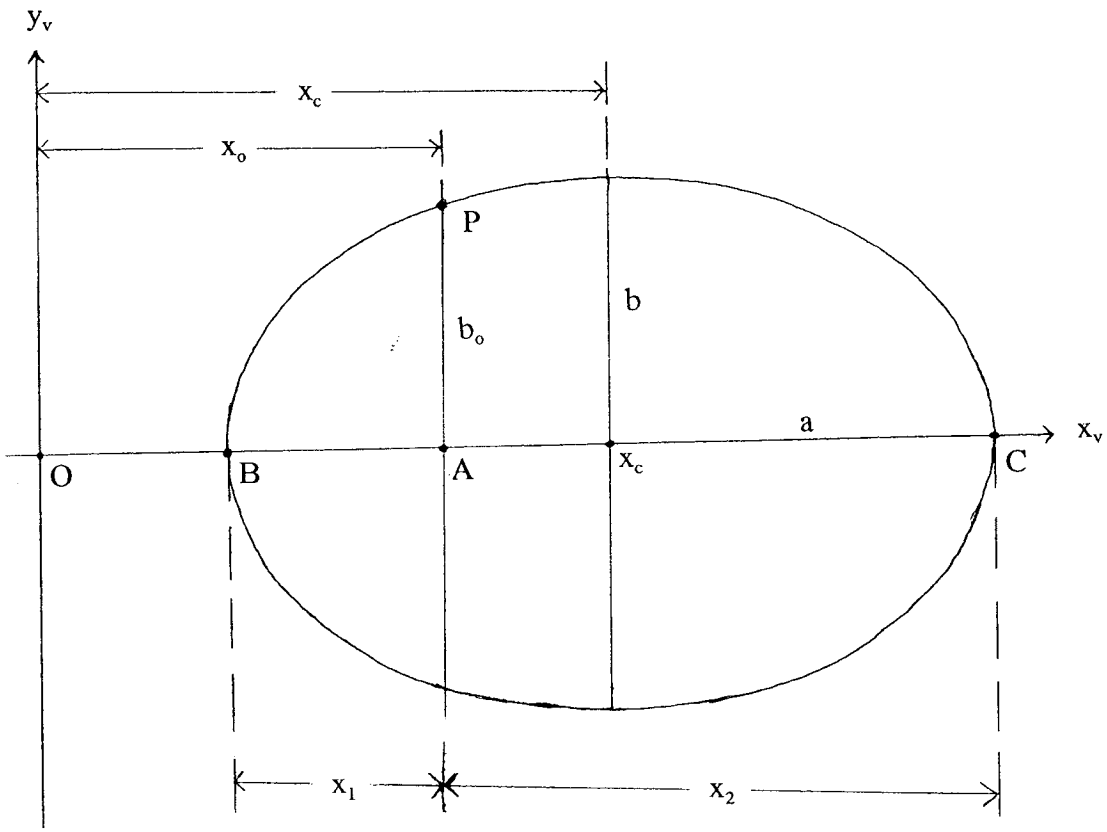

Figure 3

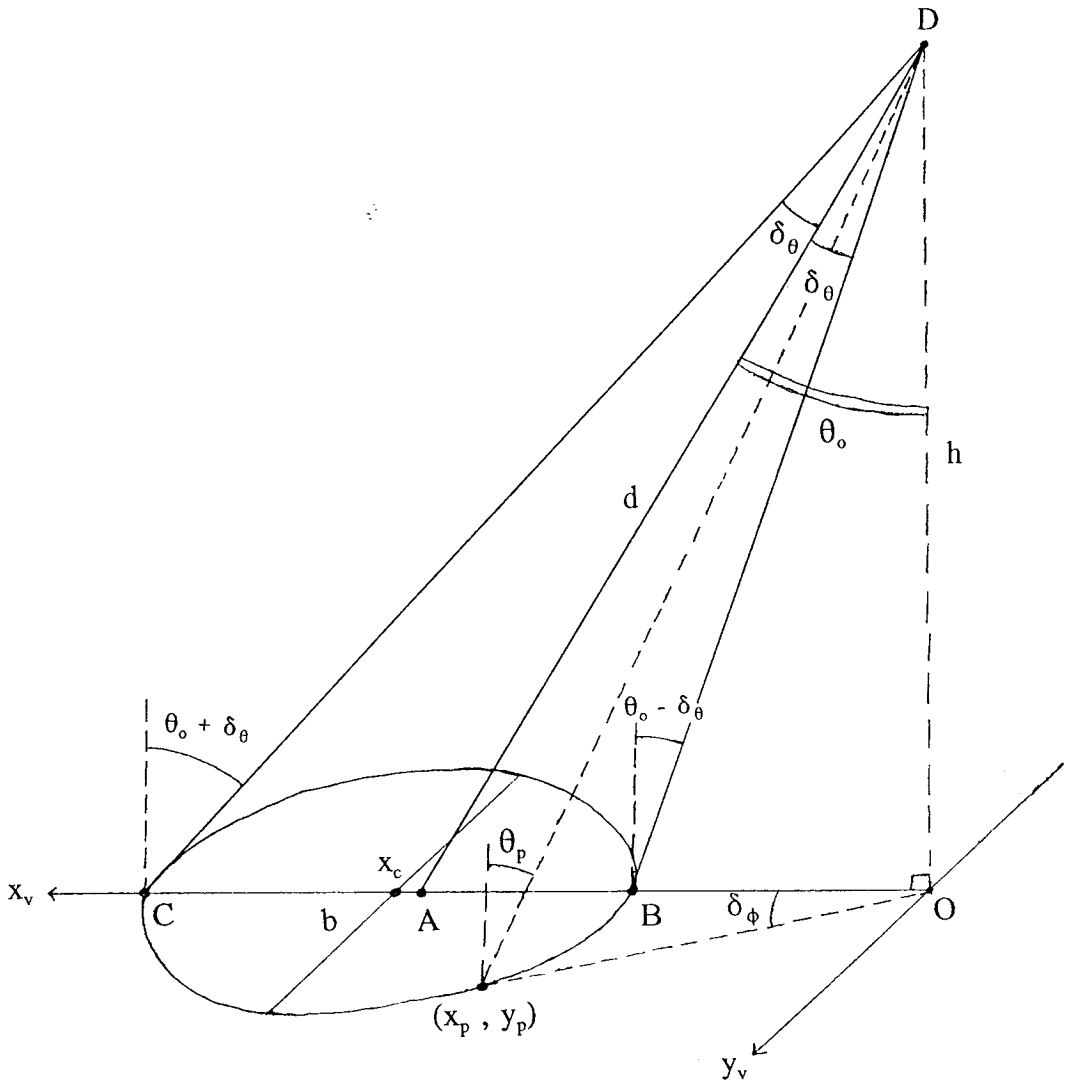
D
δ_θ
δ_θ
θ_o
h
d
$\theta_o + \delta_\theta$
$\theta_o - \delta_\theta$
θ_p
x_c
x_v
C
b
A
B
δ_ϕ
O
(x_p , y_p)
y_v

Figure 4

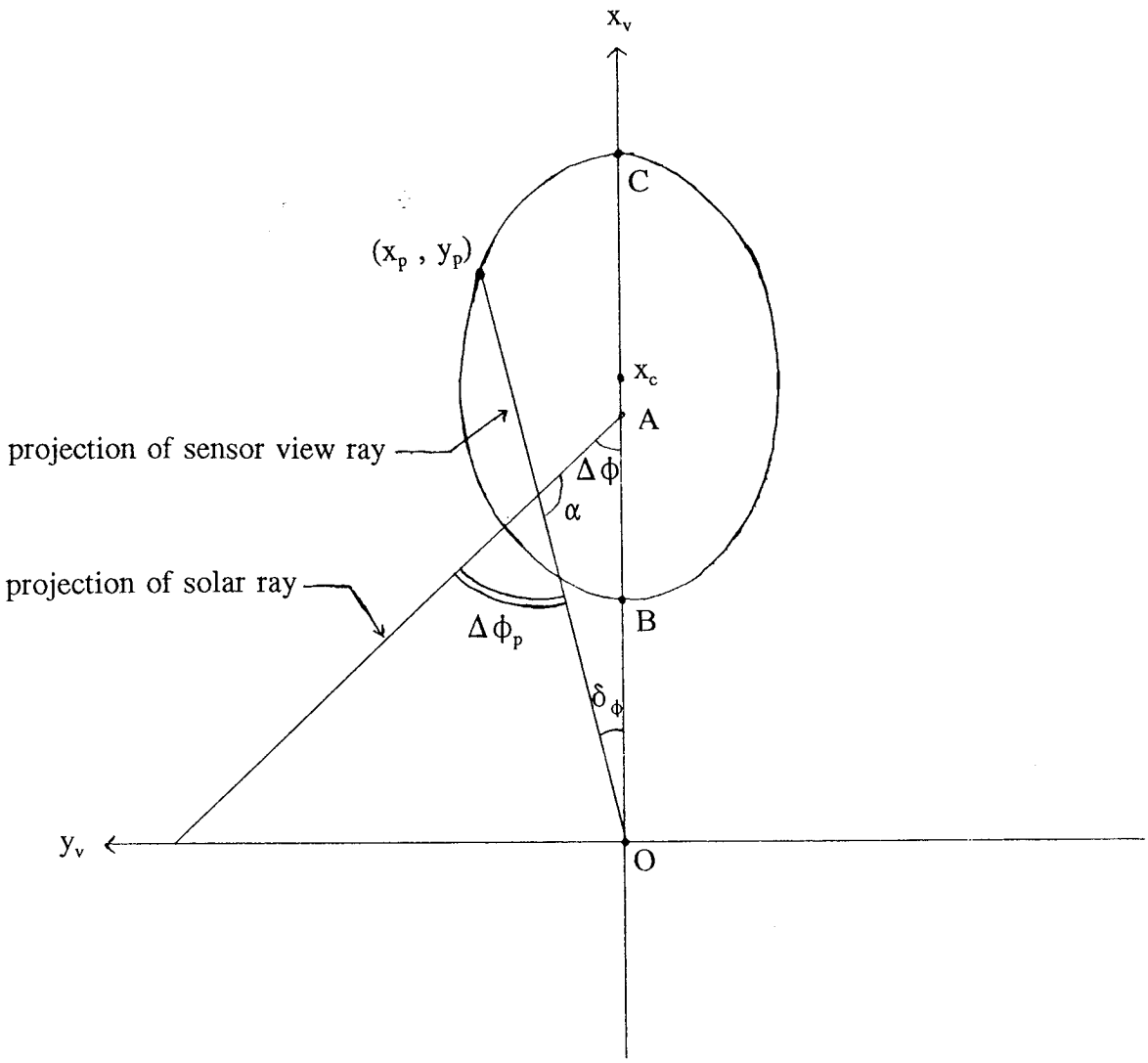
x_v
C
(x_p , y_p)
x_c
A
projection of sensor view ray
$\Delta\phi$
α
projection of solar ray
$\Delta\phi_p$
B
δ_ϕ
y_v
O

Figure 5